Published in *International Journal of Solids and Structures* (2021) **210–211**, 255-272
doi: https://doi.org/10.1016/j.ijsolstr.2020.11.006

Dispersion of rigid line inclusions as stiffeners and shear band instability triggers

M. Goudarzi[a,*], F. Dal Corso[b], D. Bigoni[b], A. Simone[c,a]

[a] *Faculty of Civil Engineering and Geosciences, Delft University of Technology, Delft, the Netherlands*
[b] *Department of Civil, Environmental and Mechanical Engineering, University of Trento, Trento, Italy*
[c] *Department of Industrial Engineering, University of Padova, Padua, Italy*

Dedicated to Professor Henryk Petryk on the occasion of his 70th birthday

Abstract

A dispersion of stiff and thin ('rigid line') inclusions (RLIs) in a matrix material may result beneficial for stiffening in the elastic range, but might be detrimental to strength, as material instabilities may be triggered by inclusions when the matrix is brought to a viscoplastic-damaging state. This dual role of RLIs is investigated by means of the embedded reinforcement model. Validated against available analytical predictions, this numerical model is employed to assess the roles of RLIs' orientation, interaction, volume fraction, and distribution, considering up to 1500 inclusions. When the matrix material deforms inelastically, RLIs produce stress concentrations that promote the nucleation of shear bands. These are characterized at collapse for many distributions of RLIs, showing that their effects range from almost negligible to a disrupting alteration of the dominant failure mechanism. In the latter case, it is shown that the dominant shear bands can be fragmented by RLIs into a mosaic of tiny localization bands. These results offer new insights into energy dissipation mechanisms of reinforced materials, as they are promoted or inhibited by the interactions of rigid line inclusions.

Keywords: rigid line inclusions, material instability, shear band formation, embedded reinforcement model, finite element method

1. Introduction

Biological nanocomposites with stiff minerals embedded in a relatively soft protein-based bulk material (Landis, 1995), polymer nanocomposites with platelet-like clay particles (Kojima et al., 1993), cermets (Clyne and Withers, 1995), and graphene-based composite materials (Hu et al., 2014; Stankovich et al., 2006) are some instances of composites where the reinforcing agents are so thin and so much stiffer than the hosting material that they can be effectively modeled as rigid-line elements. Such composites and the roles of the highly stiff phase on their mechanical responses can, in principle, be studied with available numerical models. However, these analyses would face inevitable limitations connected to the computational

*Corresponding author.
E-mail addresses: m.goudarzi@tudelft.nl, francesco.dalcorso@unitn.it, davide.bigoni@unitn.it, angelo.simone@unipd.it, a.simone@tudelft.nl

Published in *International Journal of Solids and Structures* (2021) **210–211**, 255-272
doi: https://doi.org/10.1016/j.ijsolstr.2020.11.006

complexity stemming from the large number of arbitrarily-oriented inclusions. A computationally affordable method is employed here to overcome this limitation and to reveal the complex mechanical interactions and the consequent localized patterns characterizing failure of ductile materials containing rigid inclusion dispersions.

The numerical analysis of composites characterized by realistic volume fractions of inclusions with high aspect ratio has been mainly hindered by the requirement of conformal discretizations, an issue strictly inherent to classical finite element methods. A further complication arises when the interface between inclusion and matrix material is regarded as imperfect – namely, involving discontinuities in relative displacements which may be represented by means of interface elements requiring *ad-hoc* meshing procedures. Broadly speaking, aspects such as large number of inclusions and interfacial conditions can be adequately addressed with the standard finite element method (FEM), only when the number of inclusions is moderate. In contrast, these FEM methodologies reach their limits at high inclusion density, as the simulation cost can become very high (an example of such a situation with perfectly bonded fibers discretized as cylinders in a three-dimensional space can be found in Lusti and Gusev (2004)). With reference to platelet-shaped inclusions, simplifying modeling assumptions rely on various dimensional reduction procedures, the most common being the two-dimensional projection of the problem geometry, followed, when possible, by a further dimensional reduction due to the high aspect ratio of the projection. The former is an accepted simplification in the numerical analysis of polymer-clay nanocomposites, where the elongated rectangular cross section of clay platelets is discretized by means of a conformal two-dimensional mesh (Sheng et al., 2004). The latter simplification consists in the reduction of the narrow two-dimensional rectangular projection into a one-dimensional line inclusion, as conveniently done by Sanborn and Prévost (2008). This approach is also pursued in rigid line inclusion (RLI) models, which essentially are two-dimensional analytical models describing a rigid inclusion embedded in a deformable planar matrix (Atkinson, 1973; Baranova et al., 2020; Chen, 1986, 1991; Wang and Schiavone, 2019; Wang et al., 1985). Incidentally, it is worth noting the three-dimensional analytical work by Chaudhuri and Chiu (Chaudhuri, 2012; Chaudhuri and Chiu, 2012) dealing with planar rigid inclusions.

In a two-dimensional setting, to which the present work is limited, line inclusions can be discretized by means of finite elements traditionally employed for the analysis of (fiber-)reinforced concrete or composites (for example, a bar or a beam element surrounded by continuum elements) in an adequate manner. In doing so, however, a problem arises from the conformal discretization of matrix and inclusion, an issue that has been addressed with a number of different strategies: (i.) embedded reinforcement models (Balakrishnan and Murray, 1986; Barzegar and Maddipudi, 1997; Cunha et al., 2012; Elwi and Hrudey, 1989; Hartl, 2002; Zhang et al., 2020; Zienkiewicz et al., 1972), (ii.) lattice models (Bolander and Saito, 1997; Cusatis et al., 2011; Kozicki and Tejchman, 2010), (iii.) boundary integral equation formulations and boundary element methods (Chatterjee et al., 2008; Dong and Lee, 2005; Nishimura and Liu, 2004), (iv.) partition of unity enrichment techniques (Pike and Oskay, 2015; Pike et al., 2015; Radtke et al., 2010), (v.) non-matching immersed methods (Alzetta and Heltai, 2020), (vi.) interface-constraint methods (Auricchio et al., 2017), and (vii.) other mesh-free approaches (Barbieri and Pugno, 2015; Yaghoobi and Chorzepa, 2015). A characterizing feature of all these methods is that line inclusions can be placed in the computational domain independently of the matrix domain discretization, thereby overriding the need for conformal discretizations. Among these approaches, embedded reinforcement models are the closest to a classical FEM technique in terms of implementation and offer a good compromise between accuracy and computational burden, making them ideal tools for the characterization of dense inclusion distributions.

This article shows that the mechanics of composites with dense RLIs' distributions can be adequately modeled by means of the cited embedded reinforcement approach. This approach is introduced in Section 2.2

Published in *International Journal of Solids and Structures* (2021) **210–211**, 255-272
doi: https://doi.org/10.1016/j.ijsolstr.2020.11.006

with reference to elastic inclusions imperfectly connected to the matrix material (detailed in Section 2.3). The study reported in Section 2.4 indicates that RLIs can be properly represented by tuning the interfacial and inclusion stiffness parameters, showing in this way that linear elastic fields predicted by analytical solutions (Atkinson, 1973; Chen, 1986, 1991; Wang et al., 1985) can be correctly approximated. Analogies and distinctive features are highlighted with the corresponding fields relevant to cracks (Bigoni et al., 2008; Dal Corso et al., 2008; Misseroni et al., 2014; Noselli et al., 2010). Sections 3 and 4 show that rigid line inclusions can be subject to conditions of stress annihilation and neutrality (Atkinson, 1973; Dal Corso et al., 2016a,b; Wang et al., 1985). These examples are complemented in Sections 3 and 4 by a detailed micromechanical analysis on the role of inclusion orientation and interaction.

This work also addresses another important aspect related to RLIs. A common manifestation of failure in a ductile material is through the nucleation and growth of shear bands, which represent localized regions of intense shearing strain, typically occurring at severe plastic deformation. This phenomenon is an example of material instability (a problem thoroughly investigated by H. Petryk (Bigoni and Petryk, 2002; Petryk, 1989, 1991, 1992, 1997, 2000, 2020; Petryk and Stupkiewicz, 2012), to whom this article is dedicated) and may be theoretically explained in terms of the loss of ellipticity of the incremental constitutive tensor which, in a continuous deformation path, is detected when the acoustic tensor (corresponding to the loading branch of the constitutive operator) loses positive definiteness (Bigoni, 2012). Both experimental evidence (Misra and Mandal, 2007; Özturk et al., 1991) and theoretical modelling (Argani et al., 2013; Bigoni et al., 2008) demonstrate that, compared to the situation of a uniform material, inhomogeneities in the form of rigid inclusions induce in the surrounding material a severe stress concentration, which strongly promotes the nucleation and growth of shear bands and changes the failure mechanisms. Therefore, if on the one hand inclusions stiffen the overall response of a solid, on the other they may become even detrimental to strength in the case of brittle matrices. This effect has been experimentally evaluated for brittle matrix material in Noselli et al. (2010), Misseroni et al. (2014), and Dal Corso et al. (2008) on resin specimens reinforced with thin metal laminae, where the latter were shown to induce premature failure. In composites with complex distributions of several inclusions it is expected that the presence of the latter influences not only the nucleation of shear bands, but also their growth. In fact, the presence of a shear band strongly modifies the mechanical state, and, in particular, the state of stress and strain tend to, say, 'propagate' along it, up to a long distance from the nucleation site.

Influenced by the geometry of the inclusions' distribution and, at the same time, by the strong directionality and symmetry of the shear band phenomenon, networks of shear bands with higher or smaller degree of regularity are expected to form, affecting the response of the material at failure through overall ductility and dissipation mechanisms that are different from those measured in the matrix material. An important objective of the present study is to investigate the formation of shear bands networks when the matrix material is ductile and complex distributions of a large number of RLIs are present. Shear band formation and interaction is analyzed in Section 4 in an elastic-viscoplastic-damage material matrix containing various distributions of rigid line inclusions. As anticipated, the interest in this analysis lies in the fact that experimental and analytical evidences indicate that the role of a RLI changes from reinforcing agent into source of material instability (Bigoni et al., 2008; Dal Corso and Bigoni, 2009; Misra and Mandal, 2007; Özturk et al., 1991) nucleating strain localization which in turn leads to the definition of a failure mechanism. The analyses proposed in this work show how shear bands are generated near the tips of inclusions and 'self-organize' in 'mosaic' geometric pattern, which can promote or limit the near failure energy dissipation.

Published in *International Journal of Solids and Structures* (2021) **210–211**, 255-272
doi: https://doi.org/10.1016/j.ijsolstr.2020.11.006

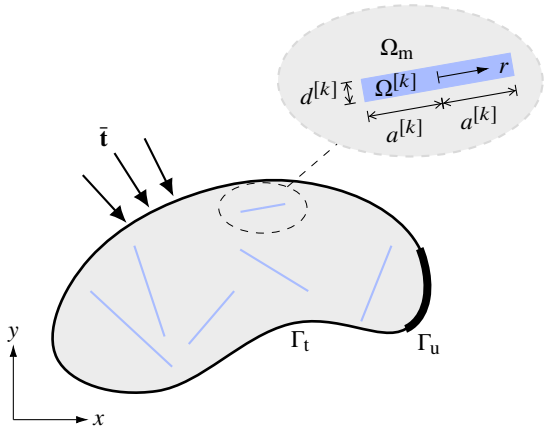

Figure 1: Two-dimensional schematic of a solid containing rigid line inclusions.

2. Method of analysis

The main assumptions, the numerical and constitutive models employed in this study are summarized. In particular, the dimensionally-reduced model representing the rigid line inclusions is validated against representative analytical results.

2.1. Domain and inclusion approximations

Consider a solid with uniform properties across its thickness h, embedding M thin, elongated, and rigid inclusions, all with a $2a^{[k]} \times d^{[k]} \times h$ parallelepiped shape (the index $k = 1, ..., M$ selects the specific inclusion). All inclusions' edges of length h are aligned parallel to the out-of-plane direction z. The solid thickness h may be small or large, so that a plane stress or plane strain condition prevails in the $x - y$ plane, respectively. The planar section of the solid is depicted in Fig. 1. In order to be representative of a RLI, the thickness $d^{[k]}$ is much smaller than the length $2a^{[k]}$; in this way the inclusion retains a volume $(2a^{[k]}d^{[k]}h)$ and the RLI volume fraction can be defined. The $2a^{[k]} \times d^{[k]}$ rectangular cross section of an inclusion in the $x - y$ plane is shown in the inset of Fig. 1, inclined at an angle $\overline{\theta}^{[k]}$ with respect to the x-axis and centered at $x^{[k]}$ and $y^{[k]}$. In this plane, the k-th inclusion is therefore approximated by a segment occupying the one-dimensional domain $\Omega^{[k]}$

$$\Omega^{[k]} = \left\{ x, y \,\middle|\, x = x^{[k]} + r\cos\overline{\theta}^{[k]},\ y = y^{[k]} + r\sin\overline{\theta}^{[k]},\ r \in \left[-a^{[k]}, a^{[k]}\right] \right\}, \tag{1}$$

where r is the inclusion local coordinate with origin at the inclusion midpoint.

Each inclusion interacts with the surrounding bulk material through its major interfacial surface, composed by the two largest lateral surfaces, each with contact area $2a^{[k]}\,h$. The minor lateral surface, with total area $2\,d^{[k]}\,h$, is neglected as it yields a negligible contribution. For simplicity, a unit out-of-plane thickness ($h = 1$) will be henceforth assumed.

2.2. Embedded reinforcement model with slip

The embedded reinforcement model employed in this study is based on the formulation proposed by Goudarzi and Simone (2019). In embedded models, the inclusion is represented by means of an independent discretization that is superimposed to the domain discretization and equipped with a dedicated kinematic field.

Published in *International Journal of Solids and Structures* (2021) **210–211**, 255-272
doi: https://doi.org/10.1016/j.ijsolstr.2020.11.006

Next, the embedded reinforcement model is summarized with reference to a single ($M = 1$) inclusion; its extension to multiple ($M > 1$) inclusions can be readily obtained following Hartl (2002).

2.2.1. Kinematic field

In the embedded reinforcement model by Goudarzi and Simone (2019, their Section 3.1.1) the inclusion is not perfectly bonded to the surrounding bulk material. The displacement of a line inclusion consists therefore of two components: the displacement of the surrounding material and the displacement relative to it. The latter component is defined by the sliding displacement $u_{\mathrm{s}}^{[k]}$, also referred to as 'slip' in the literature, which defines a discontinuity in the displacement field across the interface between the k-th inclusion and the bulk material. The displacement $\mathbf{u}$ in the composite material is therefore defined as

$$\mathbf{u} = \begin{cases} \mathbf{u}_{\mathrm{b}} & \text{in } \Omega, \\ \mathbf{u}_{\mathrm{b}} + u_{\mathrm{s}}^{[k]} \mathbf{e}^{[k]} & \text{for } \{x, y\} \in \Omega^{[k]}, \end{cases} \tag{2}$$

where $\mathbf{u}_{\mathrm{b}}$ represents a continuous displacement field within the composite domain, and $\mathbf{e}^{[k]} = \{\cos\overline{\theta}^{[k]}, \sin\overline{\theta}^{[k]}\}$ is a unit vector tangent to the k-th inclusion line. The inclusion continuous (non-slip) component $\mathbf{u}_{\mathrm{b}} \cdot \mathbf{e}^{[k]}$ is also referred to as 'concrete' (Balakrishnan and Murray, 1986), or 'duct' (Hartl, 2002) displacement in the literature.

The relative displacement $u_{\mathrm{s}}^{[k]}$ between bulk material and the k-th inclusion calls for the definition of an appropriate interfacial constitutive law apt to describe the perfect bond between a rigid line inclusion and the surrounding bulk material; this aspect is discussed in Section 2.4.2.

2.2.2. Governing equations

With reference to the displacement field $\mathbf{u}$, Eq. (2), and considering small deformations, the principle of virtual work for a plane solid body Ω of unit thickness (Fig. 1) containing a single inclusion can be expressed as

$$\int_{\Omega\setminus\Omega^{[1]}} \nabla^{\mathrm{s}}\delta\mathbf{u}_{\mathrm{b}} : \boldsymbol{\sigma}_{\mathrm{b}}\, \mathrm{d}\Omega + d^{[1]} \int_{-a^{[1]}}^{a^{[1]}} \left(\delta\mathbf{u}_{\mathrm{b}} \cdot \mathbf{e}^{[1]}\right)_{,r} \sigma^{[1]}\, \mathrm{d}r = \int_{\Gamma_{\mathrm{t}}} \delta\mathbf{u}_{\mathrm{b}} \cdot \bar{\mathbf{t}}\, \mathrm{d}\Gamma_{\mathrm{t}}, \tag{3a}$$

$$d^{[1]} \int_{-a^{[1]}}^{a^{[1]}} \delta u_{\mathrm{s},r}^{[1]} \sigma^{[1]}\, \mathrm{d}r + 2 \int_{-a^{[1]}}^{a^{[1]}} \delta u_{\mathrm{s}}^{[1]} t^{[1]}\, \mathrm{d}r = 0, \tag{3b}$$

where the subscript '$,r$' denotes the derivative with respect to r, ∇^{s} and δ are the symmetric gradient and the first variation operators, respectively, $\boldsymbol{\sigma}_{\mathrm{b}}$ is the stress tensor in the bulk material, and the scalar $\sigma^{[1]}$ is the axial stress along the inclusion. Moreover, $\bar{\mathbf{t}}$ is the traction vector acting along the solid boundary $\Gamma_{\mathrm{t}} \subseteq \partial\Omega$, and $t^{[1]}$ is the interfacial tangential traction, acting along the inclusion-matrix interface.

Equation (3a) defines the virtual work done by the displacement field $\mathbf{u}_{\mathrm{b}}$ in the whole body, with the exception of the inclusion-matrix interface contribution. On the left-hand side, the first term represents the usual contribution of the bulk material, while the second accounts for the corresponding work in the one-dimensional inclusion domain by the duct (axial) deformation, with the factor before the integral representing the cross-sectional area $d^{[1]}\,h$ (with thickness $h = 1$). The term on the right-hand side of Eq. (3a) is the work done by the tractions applied on the boundary. Equation (3b) represents the virtual work done by the slip component of the inclusion displacement. The first term defines the work done at the boundary of the

Published in *International Journal of Solids and Structures* (2021) **210–211**, 255-272
doi: https://doi.org/10.1016/j.ijsolstr.2020.11.006

inclusion, with the factor before the integral representing the inclusion cross-sectional area $d^{[1]}\,h$. The second term accounts for the work done at the inclusion-matrix interface, defined by the two major lateral surfaces, each with area $2a\,h$. The work done across the two ends of an inclusion, each with surface $d^{[1]}\,h$, is neglected because $d^{[1]} \ll a^{[1]}$.

2.2.3. Discretization and linearizations

The discretized version of Eq. (3) at the element level for the bulk material is obtained by expressing the displacement $\mathbf{u}_\mathrm{b}$ and strain $\nabla^\mathrm{s}\mathbf{u}_\mathrm{b}$ fields as

$$\mathbf{u}_\mathrm{b} = \mathbf{N}_\mathrm{b}\mathbf{b} \qquad \text{and} \qquad \nabla^\mathrm{s}\mathbf{u}_\mathrm{b} = \mathbf{B}_\mathrm{b}\mathbf{b}, \tag{4}$$

where $\mathbf{N}_\mathrm{b}$ collects finite element nodal shape functions, $\mathbf{B}_\mathrm{b}$ the corresponding derivatives according to the displacement-strain relation, and vector $\mathbf{b}$ contains nodal displacements.

The bulk material and the line inclusion are discretized by means of two non-conforming discretizations. For convenience, the inclusion is discretized by a sequence of 2-node inclusion segments obtained from the intersection of inclusion and bulk material discretizations. The quantities below are expressed with reference to an inclusion segment with endpoints i and j. The inclusion non-slip component $\mathbf{u}_\mathrm{b}$ and its derivative $\mathbf{u}_{\mathrm{b,r}}$ are computed from the displacement field of the bulk material elements crossed by the inclusion as

$$\mathbf{u}_\mathrm{b} \cdot \mathbf{e}^{[1]} = \mathbf{N}_\mathrm{d}^{[1]}\mathbf{H}^{[1]}\mathbf{b} \qquad \text{and} \qquad \mathbf{u}_{\mathrm{b,r}} \cdot \mathbf{e}^{[1]} = \mathbf{B}_\mathrm{d}^{[1]}\mathbf{H}^{[1]}\mathbf{b}, \tag{5}$$

where the expressions for the matrices $\mathbf{N}_\mathrm{d}^{[1]}$, $\mathbf{B}_\mathrm{d}^{[1]}$, and $\mathbf{H}^{[1]}$ are reported by Goudarzi and Simone (2019). The slip component $u_\mathrm{s}^{[1]}$ and its derivative $u_{\mathrm{s},r}^{[1]}$ can be approximated as

$$u_\mathrm{s}^{[1]} = \mathbf{N}_\mathrm{s}^{[1]}\mathbf{s}^{[1]} \qquad \text{and} \qquad u_{\mathrm{s},r}^{[1]} = \mathbf{B}_\mathrm{s}^{[1]}\mathbf{s}^{[1]}, \tag{6}$$

where $\mathbf{s}^{[1]} = \left[s_i,\ s_j\right]^\mathrm{T}$ is the vector of endpoint slips, while

$$\mathbf{N}_\mathrm{s}^{[1]} = \begin{bmatrix} N_i & N_j \end{bmatrix} \qquad \text{and} \qquad \mathbf{B}_\mathrm{s}^{[1]} = \begin{bmatrix} N_{i,r} & N_{j,r} \end{bmatrix} \tag{7}$$

contain inclusion shape functions and their derivatives, respectively.

The discretized displacements, Eqs. (4) to (6), are introduced in the weak form (3) and the resulting equations can be interpreted as the equilibrium conditions

$$\mathbf{f}_\mathrm{int,b} = \bar{\mathbf{f}}_\mathrm{ext,b} \qquad \text{and} \qquad \mathbf{f}_\mathrm{int,s}^{[1]} = \bar{\mathbf{f}}_\mathrm{ext,s}^{[1]} \tag{8}$$

representing a balance between internal and external forces, related to the contributions from the bulk material and the inclusion, with

$$\begin{aligned}
\mathbf{f}_\mathrm{int,b} &= \int_{\Omega\setminus\Omega^{[1]}} \mathbf{B}_\mathrm{b}^\mathrm{T}\boldsymbol{\sigma}_\mathrm{b}\,\mathrm{d}\Omega + d^{[1]}\int_{-a^{[1]}}^{a^{[1]}} \mathbf{H}^{[1]\mathrm{T}}\mathbf{B}_\mathrm{d}^{[1]\mathrm{T}}\sigma^{[1]}\,\mathrm{d}r,\\
\bar{\mathbf{f}}_\mathrm{ext,b} &= \int_{\Gamma_\mathrm{t}} \mathbf{N}_\mathrm{b}^\mathrm{T}\bar{\mathbf{t}}\,\mathrm{d}\Gamma_\mathrm{t},\\
\mathbf{f}_\mathrm{int,s}^{[1]} &= d^{[1]}\int_{-a^{[1]}}^{a^{[1]}} \mathbf{B}_\mathrm{s}^{[1]\mathrm{T}}\sigma^{[1]}\,\mathrm{d}r + 2\int_{-a^{[1]}}^{a^{[1]}} \mathbf{N}_\mathrm{s}^{[1]\mathrm{T}}t^{[1]}\,\mathrm{d}r,\\
\bar{\mathbf{f}}_\mathrm{ext,s}^{[1]} &= \mathbf{0},
\end{aligned} \tag{9}$$

Published in *International Journal of Solids and Structures* (2021) **210–211**, 255-272
doi: https://doi.org/10.1016/j.ijsolstr.2020.11.006

where it is assumed, as shown in the last equation, that the inclusion is not subject to external forces.

The linearized version of the discretized weak form is obtained by expressing the constitutive relations for bulk and inclusion in rate form, with rate quantities identified by a superimposed dot, $(\dot{\cdot})$. The stress rate for the bulk material is therefore expressed in terms of nodal displacement velocities as

$$\dot{\boldsymbol{\sigma}}_{\mathrm{b}} = \mathbf{D}_{\mathrm{b}}\, \mathbf{B}_{\mathrm{b}}\, \dot{\mathbf{b}}, \tag{10}$$

where $\mathbf{D}_{\mathrm{b}}$ relates the stress and strain rates in the bulk material. The rate $\dot{\sigma}^{[1]}$ of the (axial) stress along the inclusion and the rate $\dot{t}^{[1]}$ of the interfacial tangential traction are defined as

$$\dot{\sigma}^{[1]} = E_{\mathrm{i}}^{[1]} \left(\mathbf{B}_{\mathrm{d}}^{[1]} \mathbf{H}^{[1]} \dot{\mathbf{b}} + \mathbf{B}_{\mathrm{s}}^{[1]} \dot{\mathbf{s}}^{[1]} \right), \qquad \dot{t}^{[1]} = K_{\mathrm{bt}}^{[1]} \mathbf{N}_{\mathrm{s}}^{[1]} \dot{\mathbf{s}}^{[1]}, \tag{11}$$

where a linear elastic behavior is assumed for the inclusion and the inclusion-matrix interface, with $E_i^{[1]}$ the Young's modulus of the inclusion and $K_{\mathrm{bt}}^{[1]}$ the interfacial stiffness. Because of the nonlinear constitutive relation of the bulk material, summarized in Section 2.3, the governing equations are solved using an incremental-iterative procedured by means of the linearized relation reported below obtained following standard procedures (Zienkiewicz and Taylor, 1989). With reference to a generic load increment, the discrete governing system of nonlinear equations is solved using the Newton-Raphson iterative solution scheme for the iterative displacements $\delta\mathbf{b}$ and $\delta\mathbf{s}^{[1]}$ according to

$$\begin{bmatrix} \mathbf{K}_{\mathrm{bb}}^{j-1} & \mathbf{K}_{\mathrm{bs}}^{[1]\,j-1} \\ \mathbf{K}_{\mathrm{sb}}^{[1]\,j-1} & \mathbf{K}_{\mathrm{ss}}^{[1]\,j-1} \end{bmatrix} \begin{bmatrix} \delta\mathbf{b}^{j} \\ \delta\mathbf{s}^{[1]\,j} \end{bmatrix} = \begin{bmatrix} \bar{\mathbf{f}}_{\mathrm{ext,b}}^{j} \\ \mathbf{0} \end{bmatrix} - \begin{bmatrix} \mathbf{f}_{\mathrm{int,b}}^{j-1} \\ \mathbf{f}_{\mathrm{int,s}}^{[1]\,j-1} \end{bmatrix}, \tag{12}$$

where j is the iteration number, and the sub-matrices read, dropping the superscript j for clarity:

$$\begin{aligned}
\mathbf{K}_{\mathrm{bb}} &= \int_{\Omega\setminus\Omega^{[1]}} \mathbf{B}_{\mathrm{b}}^{\mathrm{T}} \mathbf{D}_{\mathrm{b}} \mathbf{B}_{\mathrm{b}}\, \mathrm{d}\Omega + E_{\mathrm{i}}^{[1]} d^{[1]} \int_{-a^{[1]}}^{a^{[1]}} \mathbf{H}^{[1]\,\mathrm{T}} \mathbf{B}_{\mathrm{d}}^{[1]\,\mathrm{T}} \mathbf{B}_{\mathrm{d}}^{[1]} \mathbf{H}^{[1]}\, \mathrm{d}r, \\
\mathbf{K}_{\mathrm{bs}}^{[1]} &= E_{\mathrm{i}}^{[1]} d^{[1]} \int_{-a^{[1]}}^{a^{[1]}} \mathbf{H}^{[1]\,\mathrm{T}} \mathbf{B}_{\mathrm{d}}^{[1]\,\mathrm{T}} \mathbf{B}_{\mathrm{s}}^{[1]}\, \mathrm{d}r, \\
\mathbf{K}_{\mathrm{sb}}^{[1]} &= E_{\mathrm{i}}^{[1]} d^{[1]} \int_{-a^{[1]}}^{a^{[1]}} \mathbf{B}_{\mathrm{s}}^{[1]\,\mathrm{T}} \mathbf{B}_{\mathrm{d}}^{[1]} \mathbf{H}^{[1]} \mathrm{d}r, \\
\mathbf{K}_{\mathrm{ss}}^{[1]} &= E_{\mathrm{i}}^{[1]} d^{[1]} \int_{-a^{[1]}}^{a^{[1]}} \mathbf{B}_{\mathrm{s}}^{[1]\,\mathrm{T}} \mathbf{B}_{\mathrm{s}}^{[1]}\, \mathrm{d}r + 2K_{\mathrm{bt}}^{[1]} \int_{-a^{[1]}}^{a^{[1]}} \mathbf{N}_{\mathrm{s}}^{[1]\,\mathrm{T}} \mathbf{N}_{\mathrm{s}}^{[1]}\, \mathrm{d}r.
\end{aligned} \tag{13}$$

The integrals over $\Omega \setminus \Omega^{[1]}$ in $\mathbf{K}_{\mathrm{bb}}$ (13) and $\mathbf{f}_{\mathrm{int,b}}$ (9) are computed with reference to the domain Ω. This computational strategy implies that the contribution along the inclusion line is counted twice because of the second integrals in $\mathbf{K}_{\mathrm{bb}}$ and $\mathbf{f}_{\mathrm{int,b}}$. Nevertheless, these contributions turn out to be negligible because inclusions are assumed to be numerically equivalent to rigid as discussed in Section 2.4.2.

2.3. Constitutive models for the bulk material

For the linear elastic analyses reported in Sections 2.4 and 3, the incremental stiffness for the bulk material corresponds to the tensor of linear isotropic elasticity ($\mathbf{D}_{\mathrm{b}} = \mathbf{D}_{\mathrm{b}}^{\mathrm{el}}$).

Published in *International Journal of Solids and Structures* (2021) **210–211**, 255-272
doi: https://doi.org/10.1016/j.ijsolstr.2020.11.006

In the numerical simulations presented in Section 4, bulk material degradation is described by means of the rate-dependent isotropic elastoplastic-damage model proposed by Simone and Sluys (2004, their Section 2) and derived from the class of models proposed by Ju (1989). The coupling of damage and plasticity is introduced by means of the effective stress concept and the hypothesis of strain equivalence. The effective stress concept allows a simple algorithmic treatment of the coupled elastic-viscoplastic-damage model. The algorithmic procedure hinges on the definition of the effective stress tensor $\tilde{\boldsymbol{\sigma}}_{\mathrm{b}}$, the algorithmic tangent moduli $\tilde{\mathbf{D}}^{\mathrm{p}}$, and the equivalent plastic strain $\tilde{\kappa}$, where a superscript tilde indicates a quantity defined in the effective stress space. Accordingly, the rate-dependent effective stress tensor $\tilde{\boldsymbol{\sigma}}_{\mathrm{b}}$ is expressed as

$$\tilde{\boldsymbol{\sigma}}_{\mathrm{b}} = \frac{\boldsymbol{\sigma}_{\mathrm{b}}}{1-\omega} = \mathbf{D}_{\mathrm{b}}^{\mathrm{el}} : \boldsymbol{\varepsilon}^{\mathrm{el}} = \mathbf{D}_{\mathrm{b}}^{\mathrm{el}} : \left(\boldsymbol{\varepsilon}_{\mathrm{b}} - \boldsymbol{\varepsilon}_{\mathrm{b}}^{\mathrm{vp}}\right), \tag{14}$$

where $\boldsymbol{\sigma}_{\mathrm{b}}$ is the stress tensor, $\boldsymbol{\varepsilon}_{\mathrm{b}}$ is the total strain, $\boldsymbol{\varepsilon}_{\mathrm{b}}^{\mathrm{vp}}$ is the viscoplastic strain, ω is a scalar damage parameter ($0 \leq \omega \leq 1$) defined as

$$\omega = \alpha \left(1 - \mathrm{e}^{-\beta\tilde{\kappa}}\right), \tag{15}$$

with α and β being dimensionless parameters governing the growth of damage and subject to the constraints $0 \leq \alpha \leq 1$ and $\beta \geq 0$.

Note that the damage parameter ω, Eq. (15), will systematically be used in the following to visualize strain localization and trace shear band patterns.

Assuming small strain viscoplasticity, the total strain rate $\dot{\boldsymbol{\varepsilon}}_{\mathrm{b}}$ is additively decomposed into elastic $\dot{\boldsymbol{\varepsilon}}_{\mathrm{b}}^{\mathrm{el}}$ and viscoplastic $\dot{\boldsymbol{\varepsilon}}_{\mathrm{b}}^{\mathrm{vp}}$ contributions:

$$\dot{\boldsymbol{\varepsilon}}_{\mathrm{b}} = \dot{\boldsymbol{\varepsilon}}_{\mathrm{b}}^{\mathrm{el}} + \dot{\boldsymbol{\varepsilon}}_{\mathrm{b}}^{\mathrm{vp}}. \tag{16}$$

Under plastic flow ($\tilde{f} \geq 0$, where $\tilde{f}$ is the yield function), the viscoplastic strain rate is expressed in the associative form according to the model introduced by Perzyna as

$$\dot{\boldsymbol{\varepsilon}}_{\mathrm{b}}^{\mathrm{vp}} = \frac{1}{\tau}\, \tilde{\phi}\left(\tilde{f}\right)\ \tilde{f}_{\boldsymbol{\sigma}}, \tag{17}$$

where τ is the relaxation time and $\tilde{f}_{\boldsymbol{\sigma}} = \partial \tilde{f} / \partial \tilde{\boldsymbol{\sigma}}_{\mathrm{b}}$.

The overstress function $\tilde{\phi}\left(\tilde{f}\right)$ is expressed in the power-law form

$$\tilde{\phi}\left(\tilde{f}\right) = \left\langle \frac{\tilde{f}}{\bar{\sigma}_0} \right\rangle^N, \tag{18}$$

where N ($N \geq 1$) is a real number and $\bar{\sigma}_0$ is the initial yield stress. The softening rule governing the yield stress is described by means of the relation

$$\bar{\sigma}\left(\tilde{\kappa}\right) = \bar{\sigma}_0 \left((1+c)\,\mathrm{e}^{-b\tilde{\kappa}} - c\mathrm{e}^{-2b\tilde{\kappa}}\right), \tag{19}$$

where b and c are dimensionless model parameters.

Following standard procedures, detailed by Simone and Sluys (2004, their Section 2), the consistent tangent operator $\mathbf{D}_{\mathrm{b}}$ for the elastic-viscoplastic-damage model can be expressed as

$$\mathbf{D}_{\mathrm{b}} = (1-\omega)\,\tilde{\mathbf{D}}^{\mathrm{p}} - \frac{\partial \omega}{\partial \tilde{\kappa}}\, \tilde{\boldsymbol{\sigma}}_{\mathrm{b}} \otimes \tilde{\mathbf{r}}, \tag{20}$$

Published in *International Journal of Solids and Structures* (2021) **210–211**, 255-272
doi: https://doi.org/10.1016/j.ijsolstr.2020.11.006

where the consistent tangent for the viscoplastic contribution assumes the form

$$\tilde{\mathbf{D}}^{\mathrm{p}} = \tilde{\mathbf{R}} - \frac{\tilde{\mathbf{R}} : \tilde{f}_{\sigma} \otimes \tilde{f}_{\sigma} : \tilde{\mathbf{R}}}{\tilde{f}_{\sigma} : \tilde{\mathbf{R}} : \tilde{f}_{\sigma} - \tilde{f}_{\kappa}\tilde{\kappa}_{\lambda} + \tau / \left(\Delta t \tilde{\phi}_{\tilde{f}}\right)} \tag{21}$$

with

$$\tilde{\mathbf{R}} = \left(\mathbf{I} + \Delta\tilde{\lambda}\mathbf{D}^{\mathrm{el}}\tilde{f}_{\sigma\sigma}\right)^{-1}\mathbf{D}^{\mathrm{el}}, \tag{22}$$

where $\tilde{f}_{\sigma\sigma} = \partial\tilde{f}_{\sigma}/\partial\tilde{\sigma}_{\mathrm{b}}$, $\tilde{f}_{\kappa} = \partial\tilde{f}/\partial\tilde{\kappa}$, $\tilde{\kappa}_{\lambda} = \partial\tilde{\kappa}/\partial\tilde{\lambda}$, being $\tilde{\lambda}$ the plastic multiplier, Δt the time increment, and $\mathbf{I}$ the fourth-order symmetrization tensor, $I_{ijkl} = \frac{1}{2}\left(\delta_{ik}\delta_{jl} + \delta_{il}\delta_{jk}\right)$.

Finally, the second-order tensor $\tilde{\mathbf{r}}$, introduced in Eq. (20), is defined as

$$\tilde{\mathbf{r}} = \frac{\tilde{\mathbf{R}} : \tilde{f}_{\sigma}}{\tilde{f}_{\sigma} : \tilde{\mathbf{R}} : \tilde{f}_{\sigma} - \tilde{f}_{\kappa}\tilde{\kappa}_{\lambda} + \tau / \left(\Delta t \tilde{\phi}_{\tilde{f}}\right)}. \tag{23}$$

2.4. Validation of the numerical model in linear elasticity

The numerical model is validated in linear elasticity. To this end, the elastic constitutive parameters for the inclusion are calibrated to reproduce the analytical solution of a single RLI embedded in an unbounded linear elastic domain. The procedure is then validated against a representative case with two collinear RLIs having the same length. Henceforth, the superscript indicating the inclusion number is omitted for clarity.

2.4.1. A summary of linear elastic analytical results

Basic concepts and analytical solutions in plane elasticity are briefly reviewed for RLIs. For convenience, a local reference system $\hat{x} - \hat{y}$ is introduced, centered at the midpoint of the RLI and with the $\hat{x}$-axis defined by the unit vector $\mathbf{e}$ aligned parallel to the inclusion as shown in Fig. 2(a).

Asymptotic stress field and stress intensity factors. Figure 2(a) shows a RLI embedded in an infinite elastic isotropic domain. The asymptotic stress field near the tip of an inclusion is expressed as (Atkinson and Craster, 1995)

$$\begin{aligned}
\sigma_{\hat{x}\hat{x}}(\rho,\phi) &= \frac{\mathcal{K}_{\mathrm{I}}^{(\varepsilon)}}{\kappa\sqrt{2\pi\rho}}\cos\frac{\phi}{2}\left(\frac{3+\kappa}{2} - \sin\frac{\phi}{2}\sin\frac{3\phi}{2}\right) + \frac{\mathcal{K}_{\mathrm{II}}^{(\varepsilon)}}{\kappa\sqrt{2\pi\rho}}\sin\frac{\phi}{2}\left(\frac{3-\kappa}{2} + \cos\frac{\phi}{2}\cos\frac{3\phi}{2}\right),\\
\sigma_{\hat{y}\hat{y}}(\rho,\phi) &= -\frac{\mathcal{K}_{\mathrm{I}}^{(\varepsilon)}}{\kappa\sqrt{2\pi\rho}}\cos\frac{\phi}{2}\left(\frac{\kappa-1}{2} - \sin\frac{\phi}{2}\sin\frac{3\phi}{2}\right) + \frac{\mathcal{K}_{\mathrm{II}}^{(\varepsilon)}}{\kappa\sqrt{2\pi\rho}}\sin\frac{\phi}{2}\left(\frac{1+\kappa}{2} - \cos\frac{\phi}{2}\cos\frac{3\phi}{2}\right),\\
\sigma_{\hat{x}\hat{y}}(\rho,\phi) &= \frac{\mathcal{K}_{\mathrm{I}}^{(\varepsilon)}}{\kappa\sqrt{2\pi\rho}}\sin\frac{\phi}{2}\left(\frac{1+\kappa}{2} + \cos\frac{\phi}{2}\cos\frac{3\phi}{2}\right) + \frac{\mathcal{K}_{\mathrm{II}}^{(\varepsilon)}}{\kappa\sqrt{2\pi\rho}}\cos\frac{\phi}{2}\left(\frac{\kappa-1}{2} + \sin\frac{\phi}{2}\sin\frac{3\phi}{2}\right),
\end{aligned} \tag{24}$$

where ρ is the distance from the inclusion tip, ϕ is the counterclockwise polar angle measured from the inclusion axis $\hat{x}$, κ is the Kolosov constant ($\kappa = 3 - 4\nu$ for plane strain and $\kappa = (3-\nu)/(1+\nu)$ for plane stress, with ν the Poisson's ratio), and $\mathcal{K}_{\mathrm{I}}^{(\varepsilon)}$ and $\mathcal{K}_{\mathrm{II}}^{(\varepsilon)}$ are, respectively, the mode I and mode II RLI stress intensity factors (SIFs) defined as (Noselli et al., 2010)

$$\mathcal{K}_{\mathrm{I}}^{(\varepsilon)} = 2\mu\lim_{\rho\to 0}\sqrt{2\pi\rho}\varepsilon_{\hat{x}\hat{x}}(\rho,\phi=0) \qquad \text{and} \qquad \mathcal{K}_{\mathrm{II}}^{(\varepsilon)} = \frac{4\kappa\mu}{\kappa-1}\lim_{\rho\to 0}\sqrt{2\pi\rho}\varepsilon_{\hat{x}\hat{y}}(\rho,\phi=0), \tag{25}$$

Published in *International Journal of Solids and Structures* (2021) **210–211**, 255-272
doi: https://doi.org/10.1016/j.ijsolstr.2020.11.006

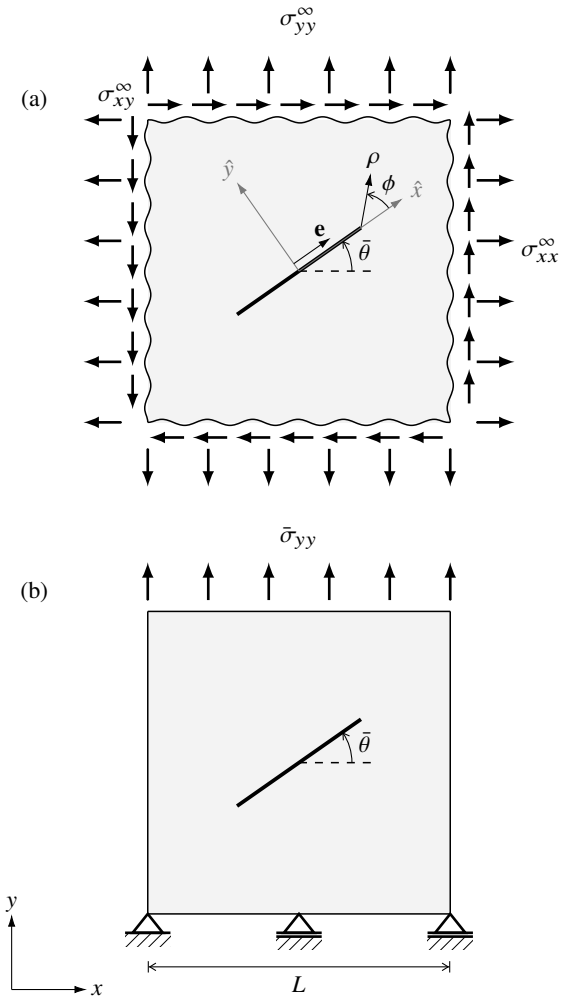

Figure 2: The two elastic boundary value problems used for the validation of the numerical model: (a) One RLI is embedded in an infinite elastic domain, and (b) the same RLI lies within a square domain of side L. The analytical solution of the elastic boundary value problem in panel (a) is used to validate the numerical model applied to the boundary value problem in panel (b). The unit vector $\mathbf{e} = \{\cos\bar{\theta}, \sin\bar{\theta}\}$ is aligned parallel to the inclusion line.

Published in *International Journal of Solids and Structures* (2021) **210–211**, 255-272
doi: https://doi.org/10.1016/j.ijsolstr.2020.11.006

where μ is the elastic shear modulus, and the superscrit (ε) highlights that the stress intensity factor is based on a strain measure, instead of a stress measure as in fracture mechanics. The asymptotic expansion (24) displays a square-root singularity in the radial direction from the inclusion tip.

J-integral. Introduced by Cherepanov (1967) and Rice (1968) in fracture mechanics, the J-integral,

$$J = \int_\Gamma \left(U \, \mathrm{d}\hat{y} - \boldsymbol{T} \cdot \frac{\partial \boldsymbol{u}}{\partial \hat{x}} \, \mathrm{d}s \right), \tag{26}$$

turns out to be path-independent also when computed for a RLI. In this expression, U is the elastic strain energy density, $\boldsymbol{T}$ is the surface traction vector, $\boldsymbol{u}$ is the displacement vector, and Γ is any closed counterclockwise contour enclosing the inclusion tip. With the asymptotic expansions (24), the J-integral expression reduces to

$$J = -\frac{1+\kappa}{8\kappa\mu} \left[\left(\mathcal{K}_{\mathrm{I}}^{(\varepsilon)} \right)^2 + \left(\mathcal{K}_{\mathrm{II}}^{(\varepsilon)} \right)^2 \right], \tag{27}$$

which, unlike the J-integral for fracture problems, is always non positive (with the physical meaning that a reduction in length of the RLI would lead to a decrease of the total potential energy). It is therefore interesting to investigate the vanishing condition for the J-integral as it defines 'neutral RLI orientations' that correspond to a homogeneous stress state, in which case the RLI leaves the stress field unperturbed. Such a condition is defined by

$$\text{neutrality condition:} \qquad \mathcal{K}_{\mathrm{I}}^{(\varepsilon)} = \mathcal{K}_{\mathrm{II}}^{(\varepsilon)} = 0 \qquad \Leftrightarrow \qquad J = 0. \tag{28}$$

A single inclusion embedded in an infinite elastic domain subject to uniform remote stress condition. Consider a single RLI of half-length a. The inclusion is inclined at an angle $\bar{\theta}$ with respect to the x axis and is embedded in an infinite elastic domain subject to a uniform remote stress field with components σ_{xx}^∞, σ_{yy}^∞ and σ_{xy}^∞ (Fig. 2(a)). The stress field ahead of the RLI has been obtained by Atkinson (1973) using a complex potentials technique and reads as, for $|\hat{x}| > a$,

$$\begin{aligned}
\sigma_{\hat{x}\hat{x}}(\hat{x}, \hat{y}=0) &= -(\kappa+3) \, \frac{\mu \, \varepsilon_{\hat{x}\hat{x}}^\infty}{\kappa} \left(1 - \frac{|\hat{x}|}{\sqrt{\hat{x}^2 - a^2}} \right), \\
\sigma_{\hat{y}\hat{y}}(\hat{x}, \hat{y}=0) &= (\kappa-1) \, \frac{\mu \, \varepsilon_{\hat{x}\hat{x}}^\infty}{\kappa} \left(1 - \frac{|\hat{x}|}{\sqrt{\hat{x}^2 - a^2}} \right), \\
\sigma_{\hat{x}\hat{y}}(\hat{x}, \hat{y}=0) &= \sigma_{\hat{x}\hat{y}}^\infty,
\end{aligned} \tag{29}$$

with

$$\begin{aligned}
\varepsilon_{\hat{x}\hat{x}}^\infty &= \frac{(\kappa+1)\sigma_{\hat{x}\hat{x}}^\infty + (\kappa-3)\sigma_{\hat{y}\hat{y}}^\infty}{8\mu}, & \sigma_{\hat{x}\hat{x}}^\infty &= \sigma_{xx}^\infty \cos^2\bar{\theta} + \sigma_{yy}^\infty \sin^2\bar{\theta} + \sigma_{xy}^\infty \sin 2\bar{\theta}, \\
\sigma_{\hat{y}\hat{y}}^\infty &= \sigma_{xx}^\infty \sin^2\bar{\theta} + \sigma_{yy}^\infty \cos^2\bar{\theta} - \sigma_{xy}^\infty \sin 2\bar{\theta}, & \sigma_{\hat{x}\hat{y}}^\infty &= -(\sigma_{xx}^\infty - \sigma_{yy}^\infty) \sin\bar{\theta}\cos\bar{\theta} + \sigma_{xy}^\infty \cos 2\bar{\theta}.
\end{aligned} \tag{30}$$

Using the above expressions, the SIFs (25) at the RLI tips can be expressed as (Noselli et al., 2010)

$$\mathcal{K}_{\mathrm{I}}^{(\varepsilon)\infty} = 2\mu\varepsilon_{\hat{x}\hat{x}}^\infty \sqrt{\pi a}, \qquad \mathcal{K}_{\mathrm{II}}^{(\varepsilon)\infty} = 0, \tag{31}$$

where the superscript '∞', added to $\mathcal{K}_{\mathrm{I}}^{(\varepsilon)}$ and $\mathcal{K}_{\mathrm{II}}^{(\varepsilon)}$, highlights the reference to an unbounded elastic domain.

Published in *International Journal of Solids and Structures* (2021) **210–211**, 255-272
doi: https://doi.org/10.1016/j.ijsolstr.2020.11.006

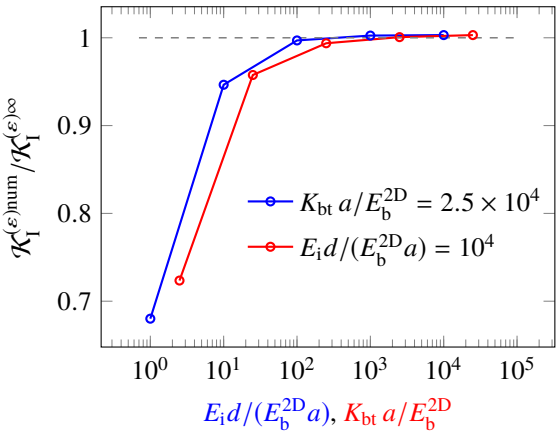

Figure 3: Convergence of the mode I stress intensity factor evaluated numerically to that estimated analytically. The two values are calculated with reference to the two boundary value problems depicted in Fig. 2 on the right (for L=10a) and on the left, respectively. The numerical solution differs from the theoretical prediction by less than 1% when $E_{\mathrm{i}}d/(E_{\mathrm{b}}^{2\mathrm{D}}a) > 100$ (blue line, with $K_{\mathrm{bt}}\,a/E_{\mathrm{b}}^{2\mathrm{D}} = 2.5\times10^{4}$) or when $K_{\mathrm{bt}}\,a/E_{\mathrm{b}}^{2\mathrm{D}} > 250$ (red line, with $E_{\mathrm{i}}d/(E_{\mathrm{b}}^{2\mathrm{D}}a) = 10^{4}$).

Neutral inclusion orientations. It is evident that the inclusion does not perturb a mechanical field whenever it lies along a zero-elongation line of an unperturbed field. In the case of an unbounded domain subject to a remote uniaxial stress state, obtained by imposing $\sigma_{yy}^{\infty} = \bar{\sigma}$ as the only non-null stress component ($\sigma_{xx}^{\infty} = \sigma_{xy}^{\infty} = 0$), the J-integral (27) reduces to

$$J = -\frac{\kappa(1+\kappa)\pi a\bar{\sigma}^2}{128\mu}\left[1 - \frac{1+2\cos 2\bar{\theta}}{\kappa}\right]^2, \tag{32}$$

and therefore the inclinations (with respect to the x-axis) $\bar{\theta} = \bar{\theta}_{\mathrm{n}}$ correspond to neutrality of the RLI when the J-integral vanishes, a condition leading to

$$\bar{\theta}_{\mathrm{n}} = \pm\frac{1}{2}\arccos\left(\frac{\kappa-1}{2}\right) \tag{33}$$

and implying $\sigma_{\hat{y}\hat{y}}^{\infty} = -(\kappa+1)/(\kappa-3)\sigma_{\hat{x}\hat{x}}^{\infty}$ and $\varepsilon_{\hat{x}\hat{x}}^{\infty} = 0$.

2.4.2. Calibration of inclusion model parameters for the numerical approximation of a RLI

The embedded reinforcement model with interfacial slip described in Section 2.2 enables the mechanical description of an imperfectly-bonded and axially compliant line inclusion in a two-dimensional domain. As such, it could be used to examine the influence of axial and bond stiffnesses. In this study we are however interested in the analysis of rigid line inclusions that are perfectly bonded to the bulk material, a situation that can be theoretically attained when $\{E_{\mathrm{i}}, K_{\mathrm{bt}}\} \to \infty$. From the computational point of view, by analyzing the stiffness matrix (13), this limit situation can be reached at sufficiently large values of the dimensionless parameters $E_{\mathrm{i}}d/(E_{\mathrm{b}}^{2\mathrm{D}}a)$ and $K_{\mathrm{bt}}\,a/E_{\mathrm{b}}^{2\mathrm{D}}$, respectively related to the axial and bond stiffness. Here and in the following the Young's modulus is defined with reference to generalized plane elasticity, $E_{\mathrm{b}}^{2\mathrm{D}}$, which corresponds to E_{b} under plane stress conditions or $E_{\mathrm{b}}/(1-\nu_{\mathrm{b}}^2)$ under plane strain conditions, where E_{b} is the three-dimensional elastic modulus.

Published in *International Journal of Solids and Structures* (2021) **210–211**, 255-272
doi: https://doi.org/10.1016/j.ijsolstr.2020.11.006

The calibration of the two dimensionless parameters $E_i d/(E_b^{2D} a)$ and $K_{bt}\, a/E_b^{2D}$, needed to obtain results pertinent to RLIs, is assessed through a comparison between $\mathcal{K}_I^{(\varepsilon)num}$, the Mode I stress intensity factor numerically derived from the J-integral (evaluated along a circular path of radius $0.1a$ and centered at the inclusion tip), and its analytical counterpart $\mathcal{K}_I^{(\varepsilon)\infty}$. To this purpose, a single horizontal ($\bar{\theta} = 0$) RLI of half-length a is considered, embedded in a linear elastic domain subject to a uniaxial remote stress $\sigma_{\hat{y}\hat{y}}^{\infty} = \bar{\sigma}_{yy}$, so that Eq. $(31)_1$, referred to Fig. 2(a) with $\bar{\theta} = 0$, simplifies to

$$\mathcal{K}_I^{(\varepsilon)\infty} = \frac{(\kappa - 3)\bar{\sigma}_{yy}\sqrt{\pi a}}{4}. \tag{34}$$

The predictions obtained with Eq. (34) are compared to results from numerical simulations referred to the boundary value problem represented in Fig. 2(b), where $\bar{\sigma}_{yy}$ is applied as a traction on the upper boundary of a square domain of size $L = 10a$. The domain is discretized with a sufficiently fine uniform mesh of bilinear elements. Plane strain conditions with Poisson's ratio $\nu_b = 0.2$ are assumed to prevail, together with $d = 0.1L$ (note that this value is immaterial since it acts as an amplification factor to E_i in the discrete set of equations). Since the inclusion is neither rigid nor perfectly bonded to the bulk material, the numerical evaluation of the J-integral (26) does not display path-independency; hence comparison with the analytical results becomes meaningful only in the case of large values for inclusion and interfacial stiffnesses.

Figure 3 shows the SIF ratio $\mathcal{K}_I^{(\varepsilon)num}/\mathcal{K}_I^{(\varepsilon)\infty}$ as a function of either $E_i d/(E_b^{2D} a)$ (blue line, with $K_{bt}\, a/E_b^{2D} = 10^4$) or $K_{bt}\, a/E_b^{2D}$ (red line, with $E_i d/(E_b^{2D} a) = 2.5 \times 10^4$). The comparison shows a relative error lower than 5% when the values of these two parameters are sufficiently large, $E_i d/(E_b^{2D} a) > 10$ or $K_{bt}\, a/E_b^{2D} > 25$. The error reduces to less than 1% when these values are above 100 and 250, respectively. With these parameter values, the inclusions can be considered as rigid in numerical simulations.

As a final remark, by assuming a sufficiently large value for the dimensionless elastic bond stiffness $K_{bt}\, a/E_b^{2D}$ between bulk material and inclusion, the embedded reinforcement model with imperfect interface practically reduces to the classical embedded reinforcement model with perfect interface (Zienkiewicz et al., 1972), whose implementation is available in standard FEM packages for the analysis of reinforced concrete structures (for instance, DIANA, ABAQUS, ANSYS).

2.4.3. Reliability assessment of the numerical model

The numerical model is validated against analytical estimates related to a single RLI embedded in a finite elastic domain and a pair of collinear RLIs in an infinite elastic domain. The case of multiple RLIs, discussed, for example, in Dong and Lee (2005), is not considered in this reliability assessment exercise. For the numerical evaluations, the inclusions are embedded in a domain of size L and the dimensionless parameters discussed in the previous section assume the values $E_i d/(E_b^{2D} a) = 10^4$ and $K_{bt}\, a/E_b^{2D} = 2.5 \times 10^4$, while the other parameters and boundary conditions are identical to those employed for the calibration of inclusion and interfacial stiffnesses. Unless otherwise stated, the computational domain of the bulk material is discretized by a sufficiently fine uniform mesh of bilinear elements.

Effects of the finiteness of the domain on the SIF. The stress intensification at the tips of a RLI of half-length a centered in a square elastic domain of size L is evaluated by varying the ratio a/L. The numerical results have been obtained with a structured mesh of bilinear elements, locally refined around the inclusion. Figure 4 shows the excellent agreement between numerical results and the semi-analytical predictions by Chen (1991) obtained with an eigenfunction expansion variational method. Worth noting is the reduction in the stress

Published in *International Journal of Solids and Structures* (2021) **210–211**, 255-272
doi: https://doi.org/10.1016/j.ijsolstr.2020.11.006

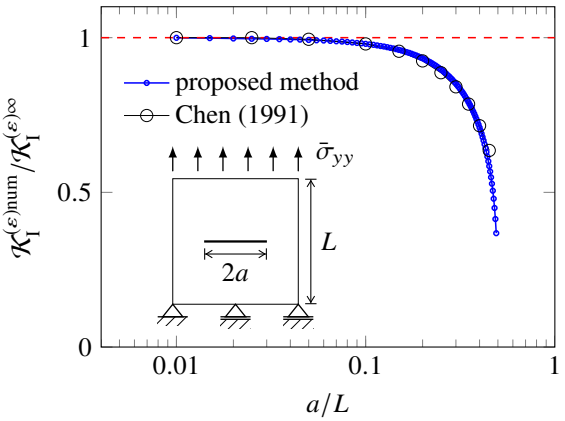

Figure 4: Effect of the finiteness of the domain size on the stress state at the tip of a RLI. The SIF for a single inclusion in a finite-size domain (Fig. 2(b)) deviates from that related to a single inclusion in an infinite domain (34) (Fig. 2(a)) when the inclusion half-length a is increased relatively to the square domain side L.

intensification at increasing values of the ratio a/L due to the interaction with the free edges. The figure also indicates that the analytical SIF value for the infinite domain $\mathcal{K}_{\mathrm{I}}^{(\varepsilon)\infty}$ is well captured when $a \leq 0.1L$.

Pair of collinear inclusions. The proposed embedded method is validated towards its exploitation in the micromechanical study of composites with large inclusion volumes, where it becomes crucial to capture interaction effects between inclusions that are otherwise neglected in available analytical estimates of elastic properties (e.g., Halpin (1969)). Although regions of stress amplification are smaller for RLIs than for cracks (Pingle et al., 2008), interactions can be quite severe for RLIs when these are placed sufficiently close to each other. Based on the duality between solutions of cracks and rigid line inclusions (Ni and Nemat-Nasser, 1996), Pingle et al. (2007) derived a relation to express the amplification of the stress intensity factors for the case of multiple RLIs embedded in an elastic unbounded domain and subject to a uniform remote stress field (with components σ_{xx}^{∞}, σ_{yy}^{∞}, and σ_{xy}^{∞}).

Two collinear (non-intersecting) inclusions are considered. The inclusions have the same half-length a and are aligned with the x-axis (which is now superimposed to the $\hat{x}$-axis because $\bar{\theta} = 0$), with their centers separated by a distance $\Delta + 2a$. In this case, considering symmetry, the SIFs, Eqs. (25), at the four RLI tips are given by

$$\mathcal{K}_{\mathrm{I}}^{(\varepsilon)}(\pm a, \Delta) = \mu\varepsilon_{xx}^{\infty}\sqrt{\frac{a}{\pi}}\int_{-1}^{1}[1 + g(\xi, \Delta/a)]\sqrt{\frac{1 \pm \xi}{1 \mp \xi}}\,\mathrm{d}\xi \quad \text{and} \quad \mathcal{K}_{\mathrm{II}}^{(\varepsilon)}(\pm a, \Delta) = 0,$$
$$\text{with } g(\xi, \Delta/a) = \frac{1}{2 - \frac{1}{2}\left(\sqrt{8 + \frac{6\Delta}{a} + \frac{\Delta^2}{a^2}} - \sqrt{\frac{2\Delta}{a} + \frac{\Delta^2}{a^2}}\right)} \frac{\xi + 2 + \frac{\Delta}{a}}{\sqrt{\left(\xi + 2 + \frac{\Delta}{a}\right)^2 - 1}}, \tag{35}$$

where $x = -a$ refers to the inner tips, namely the two closest to each other, and $x = +a$ relates to the outer tips. The analytical predictions of the two mode I SIFs (made dimensionless through division by the

Published in *International Journal of Solids and Structures* (2021) **210–211**, 255-272
doi: https://doi.org/10.1016/j.ijsolstr.2020.11.006

mode I SIF $\mathcal{K}_{\rm I}^{(\varepsilon)\infty}$, Eq. (34), relative to a single inclusion embedded within an unbounded domain as in Fig. 2(a)) are reported in Fig. 5(a) as functions of the offset ratio Δ/a. The numerical results are also reported in the figure, obtained considering the two inclusions placed in the middle of a square domain of size L (Fig. 2(b)). The domain has been discretized with a very fine mesh of bilinear elements, locally refined along the inclusion's axis. The numerical results are obtained with reference to two inclusion-domain size ratios ($a/L = \{0.05, 0.1\}$). The corresponding inclusion sizes have been used for the analytical predictions.

Figure 5(a) shows a good agreement between the numerical results and the analytical prediction by Pingle et al. (2007). Because of the influence of the finite size of the domain used in the numerical simulations, small inclusions ($a = 0.05L$) yield a better agreement between numerical and analytical results. In particular, the two inner tips show a threefold amplification of the stress intensity factor $\mathcal{K}_{\rm I}^{(\varepsilon)}$ (label A) with respect to the theoretical value $\mathcal{K}_{\rm I}^{(\varepsilon)\infty}$ corresponding to the case of a single inclusion of half-length a within an infinite plane. Finally, Fig. 5(b) shows the amplification of the numerical von Mises stress field $\sigma_{\rm vM}$ around the tips of the RLIs for an offset ratio $\Delta/a = 0.01$.

3. Rigid line inclusions as reinforcing elements: Elastic stiffening

The effective response of an elastic medium containing various distributions of up to 1500 embedded rigid line inclusions is investigated by considering RLIs distributions representative of buckypaper (i.e., carbon nanotube sheets) (Hall et al., 2008) or clay platelet (Sheng et al., 2004) nanocomposites.

Unless otherwise stated, and according to the results presented in the previous section, rigid line inclusions are modeled with $E_{\rm i}d/(E_{\rm b}^{\rm 2D}a) \approx 100$ and $K_{\rm bt}a/E_{\rm b}^{\rm 2D} \approx 250$. All the inclusions have the same size, with thickness $d = 0.0385a$ and half-length $a = 0.02L$, and are embedded in a square unit cell of size L. The mechanical properties are extracted using a computational homogenization procedure (Suquet, 1985) in which periodic boundary conditions are imposed on the two-dimensional unit cell in terms of the three average strain components representative of plane problems. The fact that a small but finite value for the RLI thickness d is retained, allows to define the volume fraction of the inclusions, which turns out to be equal to 4.62% for 1500 inclusions.

3.1. The roles of RLI orientation

The effects of RLI orientation are investigated by considering the effective response of an elastic medium characterized by a unit cell containing 1000 embedded RLIs, all inclined at the same angle $\bar{\theta}$ and with their midpoints randomly distributed in the domain as shown in Fig. 6(a). This RLIs' distribution defines an equivalent cubic symmetric solid (with cubic symmetry axes inclined at 45° with respect to the $\hat{x}$-axis aligned parallel to the RLI).

Figure 6(b) shows the effective in-plane Young's modulus $E_{{\rm eff},y}^{\rm 2D}$ parallel to the y-axis, normalized through division by the in-plane Young's modulus $E_{\rm b}^{\rm 2D}$ of the bulk material, as a function of inclusion orientation $\bar{\theta}$ for various values of the Poisson's ratio $\nu_{\rm b}$ of the bulk material, under conditions of plane stress or plane strain.

As expected, the highest value of the stiffness $E_{{\rm eff},y}^{\rm 2D}$ is attained when the inclusions are aligned parallel to the y axis ($\bar{\theta} = 90°$), with the (normalized) stiffest effective response when the bulk material has a null Poisson's ratio, $\nu_b = 0$. In addition, the effective response of the composite is stiffer than that of the bulk material for all but one specific inclination, which depends on the bulk matrix Poisson's ratio $\nu_{\rm b}$. This inclination coincides with the neutrality angle $\bar{\theta} = \bar{\theta}_{\rm n}(\nu_{\rm b})$ of a single inclusion, Eq. (33), so that the effective in-plane Young's modulus of the composite ($E_{{\rm eff},y}^{\rm 2D}$) becomes exactly that of the bulk material ($E_{\rm b}^{\rm 2D}$). Such property follows from

Published in *International Journal of Solids and Structures* (2021) **210–211**, 255-272
doi: https://doi.org/10.1016/j.ijsolstr.2020.11.006

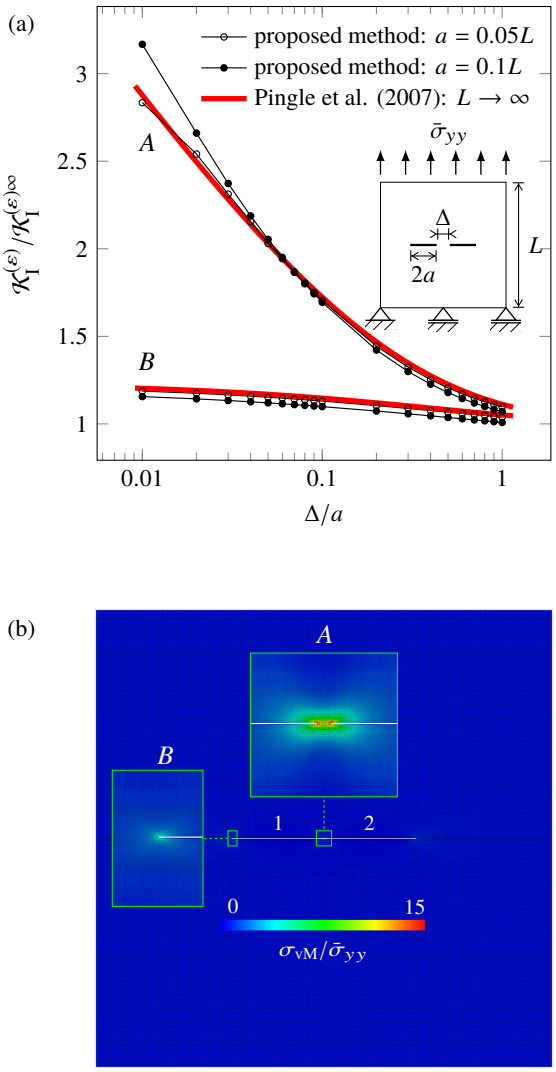

Figure 5: Interaction between two collinear rigid line inclusions aligned parallel to the x-axis and subject to a uniaxial stress field of intensity $\bar{\sigma}_{yy}$: (a) numerical and analytical stress intensity factor amplification with respect to the theoretical value $\mathcal{K}_{\mathrm{I}}^{(\varepsilon)\infty}$ for a single inclusion of half-length a at varying offset distance Δ between inclusions; (b) numerical von Mises stress field σ_{vM} around the inclusion tips for $\Delta/a = 0.01$ normalized through division by the applied stress $\bar{\sigma}_{yy}$.

Published in *International Journal of Solids and Structures* (2021) **210–211**, 255-272
doi: https://doi.org/10.1016/j.ijsolstr.2020.11.006

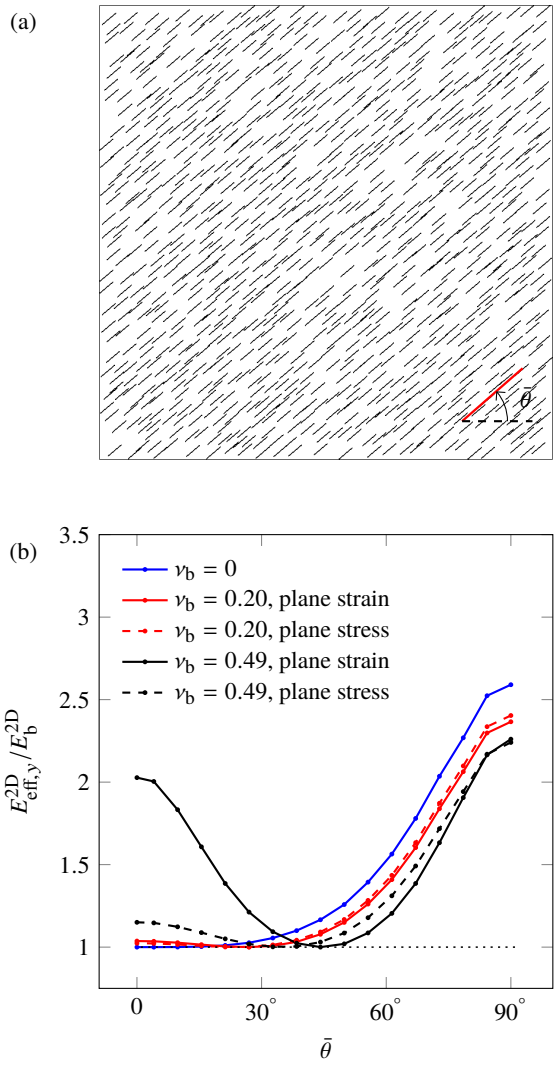

Figure 6: A square $50a \times 50a$ unit cell made up of an isotropic elastic matrix material (Young's modulus E^{2D}_{b}), containing a random distribution of 1000 equally-inclined rigid line inclusions of length $2a$ (panel (a)), leads to an equivalent cubic symmetric solid, characterized by an in-plane Young's modulus $E^{2D}_{eff,y}$ parallel to the (vertical) y-axis. This equivalent stiffness is shown in panel (b) as a function of the inclination $\bar{\theta}$ of the inclusions and for various values of the Poisson's ratio ν_b of the bulk material. Neutrality of multiple inclusions emerges at the orientation defined by Eq. (33), obtained for a single inclusion embedded in an infinite elastic domain.

Published in *International Journal of Solids and Structures* (2021) **210–211**, 255-272
doi: https://doi.org/10.1016/j.ijsolstr.2020.11.006

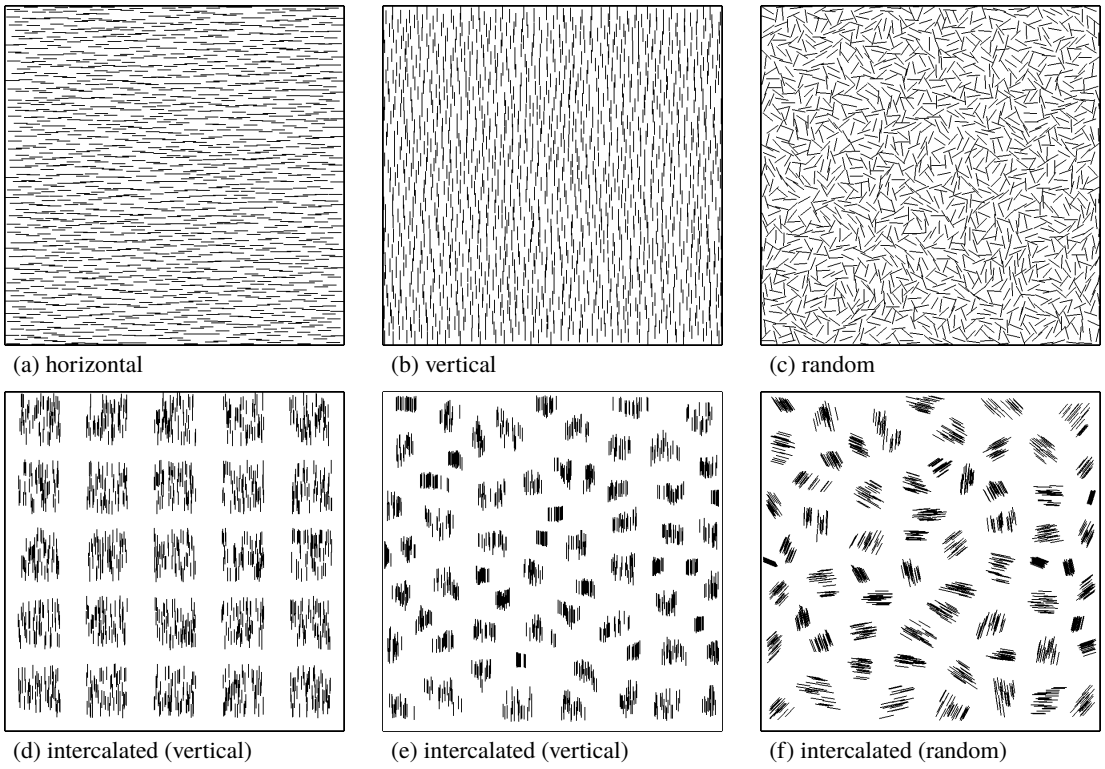

Figure 7: The roles of RLIs' distribution and volume fraction on the composite mechanical properties are assessed through the estimation of the effective Young's modulus in the vertical direction, $E^{2D}_{\text{eff},y}$. The figure shows typical RLIs' distributions for the case with 1500 inclusions of length $2a$ embedded in a square $50a \times 50a$ unit cell, corresponding to a volume fraction of 4.62%: (a) horizontal, (b) vertical, and (c) random uniformly distributed RLIs; (d, e) vertically intercalated and (f) randomly intercalated RLIs.

the neutrality condition, which automatically holds for any number of equally-inclined inclusions whenever it is satisfied for a single inclusion with that inclination.

For the special case of a nearly incompressible bulk material (with $\nu_{\text{b}} = 0.49$) under plane strain conditions, the neutral orientation $\bar{\theta}_{\text{n}}$ approaches 45°. This implies that the cubic elastic material under consideration approaches biaxially neutrality so that the effective longitudinal and transverse Young's moduli tend to the value of the bulk material (i.e., $E^{2D}_{\text{eff},x} = E^{2D}_{\text{eff},y} \approx E^{2D}_{\text{b}}$). This observation is in line with the results reported in Liu et al. (2006a), where significantly stiffened staggered biocomposites in both longitudinal and transverse directions were generated by increasing the Poisson's ratio of the soft matrix towards its incompressibility limit value.

It is finally remarked that the stiffening in the effective response for small values of the RLI inclination is significant only under both plane strain conditions and nearly incompressible bulk material, while it becomes negligible in all other cases.

3.2. The roles of RLI distribution and volume fraction

The influence of RLIs' distributions is assessed by investigating its effects on the effective in-plane Young's modulus, parallel to the y-axis $E^{2D}_{\text{eff},y}$ (reported normalized through division by E^{2D}_{b} in Fig. 8), considering the

Published in *International Journal of Solids and Structures* (2021) **210–211**, 255-272
doi: https://doi.org/10.1016/j.ijsolstr.2020.11.006

geometrical patterns of 1500 RLIs (volume fraction of 4.62%) shown in Fig. 7, with reference to the $50a \times 50a$ square unit cell. In particular, the following RLIs' distributions are analyzed (Fig. 7) when a plane stress condition prevails with Poisson's ratio $\nu_b = 0.2$:

- Uniform patterns of randomly distributed inclusions, referred to as 'exfoliated': parallel to the x-axis, panel (a), to the y-axis, panel (b), or randomly inclined, panel (c);
- Clusters of parallel inclusions arranged in a chessboard configuration, referred to as 'intercalated' and akin to distributions of clay platelets in polymer-clay nanocomposites (Liu et al., 2006b): aligned parallel to the y-axis with more, panel (d), or less, panel (e), regularity or randomly oriented clusters, panel (f).

The normalized effective Young's modulus, $E^{2D}_{\text{eff},y}/E^{2D}_b$, is reported in Fig. 8 as a function of the volume fraction of RLIs (panel (a)) and of the ratio $E_i d/(E^{2D}_b a)$ (panel (b)), for the various geometries shown in Fig. 7. Analytical predictions due to Voigt (Clyne and Hull, 2019), Halpin and Tsai (Halpin, 1969), and Mori and Tanaka (1973) are also reported for comparison in Fig. 8(b).

The results reported in Fig. 8 show that, among all the considered RLIs' distributions, the distribution of vertical inclusions (panel (b)) displays the stiffest response, with a stiffening factor of 3.8, while a negligible stiffening is observed for horizontal distributions (panel (a)).

The stiffening is reduced for clustered distributions, with an increase factor of 2 and 1.5 for the vertical distributions in panels (d) and (e), respectively. As a side remark, analytical micromechanical approaches (Halpin, 1969) and two-step homogenization schemes (Pierard et al., 2004) are insensitive to the RLIs' distribution and yield identical estimates, not reported for brevity, for composites with exfoliated and intercalated inclusions such as those reported in panels (b) and (d), respectively. Random inclusion orientations yield much softer composites, with an increase factor of 1.6 observed for the exfoliated distribution in panel (c) and 1.16 for the intercalated distribution in panel (f). Inclusions inclined at the neutral angle $\bar{\theta} \approx 24.09°$, in distributions similar to those reported in panels (a) or (b), leave the effective in-plane Young's modulus unaltered ($E^{2D}_{\text{eff},y} = E^{2D}_b$). When the vertical distribution in Fig. 7(b) is considered, a marked nonlinear increase in the elastic stiffness of the composite is displayed (Fig. 8(a), blue line) as an indication that the interaction between inclusions is maximized for this particular distribution.

Panel (b) in Fig. 8 compares numerical predictions with analytical micromechanical estimates (Voigt, Halpin-Tsai (H-T), and Mori-Tanaka (M-T)) for the distribution of 1500 vertical inclusions shown in Fig. 7(b) for various ratios $E_i d/(E^{2D}_b a)$. The agreement between numerical and analytical estimates is generally acceptable for soft inclusions. For stiff inclusions, the Voigt estimate is the less reliable and overestimates the numerical predictions and the other estimates. The numerical predictions are found in a relatively better match with Halpin-Tsai estimates, although all analytical micromechanical models are found to overestimate the effective stiffness for stiff inclusions.

4. RLIs as instability triggers: Nucleation and growth of shear bands

Shear bands emergence and propagation are numerically investigated in this section. The analysis is reffered to an elastic-viscoplastic-damage bulk material, whose constitutive model is summarized in Section 2.3 and enables an objective, mesh independent analysis when strain localization occurs. In the following, shear bands are identified by highly localized damage regions as they offer a clear evidence of strain localization. In this section 'damage localization' is used interchangeably with the term 'shear band'.

Published in *International Journal of Solids and Structures* (2021) **210–211**, 255-272
doi: https://doi.org/10.1016/j.ijsolstr.2020.11.006

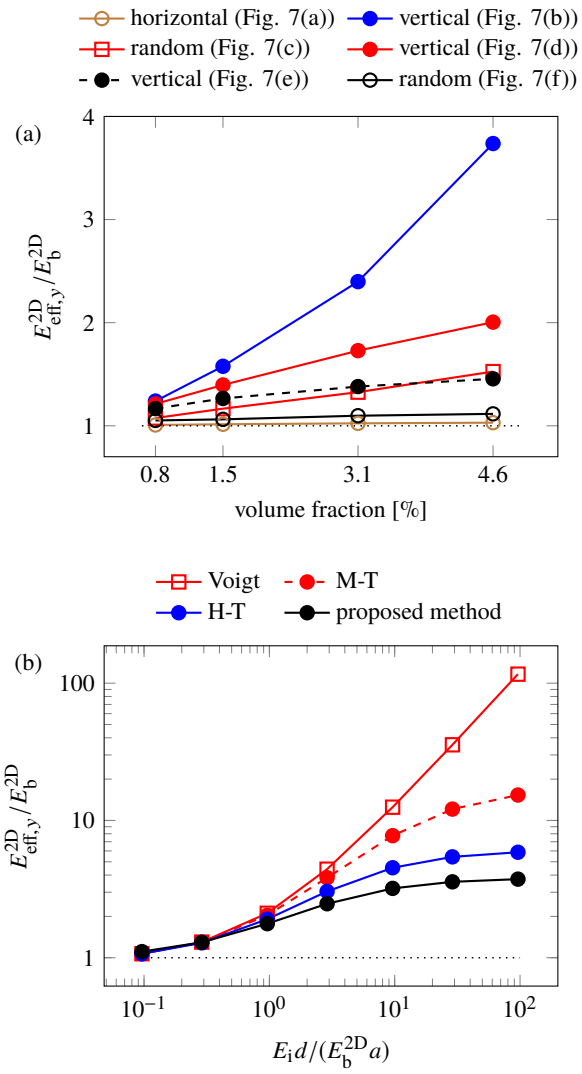

Figure 8: Predicted effective Young's modulus $E^{2D}_{\text{eff},y}$ of a composite (a) with an increasing number of RLIs for distributions similar to those shown in Fig. 7 and (b) for 1500 vertical inclusions (oriented along the y axis, Fig. 7(b)) as a function of the ratio $E_i d/(E^{2D}_b a)$. Analytical micromechanical estimates (Voigt, Halpin-Tsai (H-T), and Mori-Tanaka (M-T)) are also included.

Published in *International Journal of Solids and Structures* (2021) **210–211**, 255-272
doi: https://doi.org/10.1016/j.ijsolstr.2020.11.006

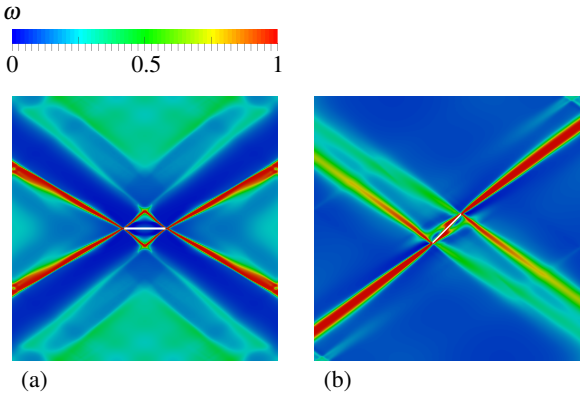

Figure 9: Localization of damage, parameter ω defined by Eq. (15), in a specimen subject to tensile stretching with an embedded rigid line inclusion inclined at angles $\bar{\theta} = 0$ (a) and $\bar{\theta} = 45°$ (b) with respect to the horizontal axis. Shear bands exhibit a double symmetry in (a), while the shear bands closer to the inclusion axis are the most intense in (b).

Quasi-static damage evolution and failure mechanisms are systematically investigated for various RLIs' distributions embedded in a square domain of size L under plane stress conditions, with Poisson's ratio $\nu_\mathrm{b} = 0.2$. Following the calibration performed in Section 2.4.2, RLIs are modeled by assuming $E_\mathrm{i} d/(E_\mathrm{b}^{2\mathrm{D}} a) = 100$ and $K_\mathrm{bt} a/E_\mathrm{b}^{2\mathrm{D}} = 250$. Material degradation is described by means of a J_2 material response with von Mises yield stress $\bar{\sigma}_0 = 10^{-4} E_\mathrm{b}^{2\mathrm{D}}$, an exponential softening rule governing the cohesion capacity of the material (Eq. (19) with $b = 200$ and $c = -1$), and an exponential damage law (Eq. (15) with parameters $\alpha = 0.99$ and $\beta = 300$). The viscoplastic model of the Perzyna type is characterized by exponent $N = 1$ in the power-law overstress function (18) and ratio $\tau/\Delta t = 8000$ in Eq. (21).

Shear bands patterns are examined and compared for various RLIs' distributions and under different boundary conditions when the load-carrying capacity of the specimens is almost exhausted, which represents the situation when failure is attained.

4.1. Only one RLI

One RLI of half-length $a = L/13$, centered in a square domain, is analyzed at various inclinations. The bottom edge of the domain is constrained as in Fig. 2(b) so that at all points (except at the leftmost corner where the displacement in both directions is prescribed to be null) the vertical displacement is constrained and the tangential tractions are set to zero. The lateral edges of the domain are left unloaded, and the top edge is displaced vertically (in the direction of the y-axis) through the imposition of a constant displacement rate $\dot{\bar{u}}_y$, until the final displacement $\bar{U} = 0.0015L$ is reached in 200 equal time-steps. The tangential tractions at the top edge are set to zero.

Figure 9 shows the damage field, expressed through parameter ω defined by Eq. (15), at an imposed displacement $\bar{u}_y = \bar{U}$ for the two inclusion angles, $\bar{\theta} = 0°$ (panel (a)) and $\bar{\theta} = 45°$ (panel (b)). A symmetric shear band formation is clearly visible, emanating from the tips of the RLI and showing two equivalent localization directions in panel (a), while shear bands are more pronounced in a specific direction when symmetry is lost (panel (b)). In the latter case, the shear band with the inclination closest to the inclusion axis is the most intense, when compared to the other conjugate direction. The numerical predictions are in agreement with analytical findings referred to the incremental theory of J_2-deformation theory of plasticity (Dal Corso

Published in *International Journal of Solids and Structures* (2021) **210–211**, 255-272
doi: https://doi.org/10.1016/j.ijsolstr.2020.11.006

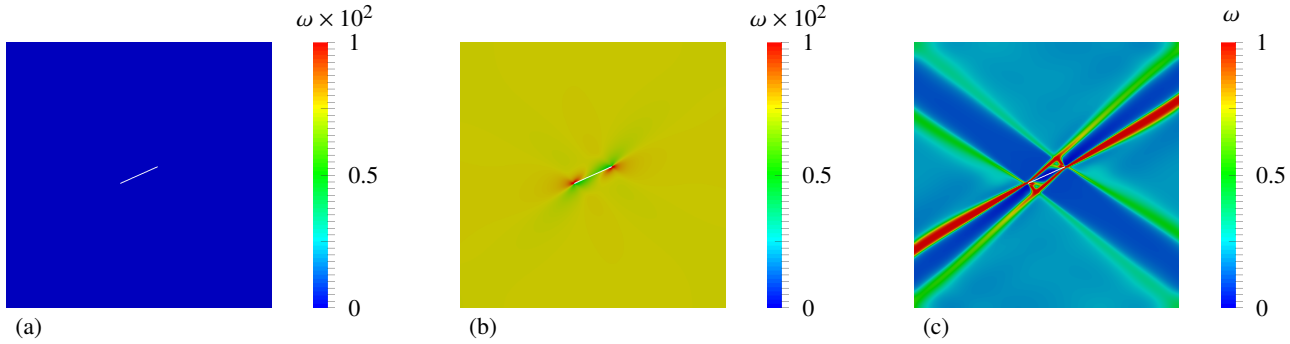

Figure 10: Evolution of the damage field ω in a specimen containing a single inclusion, inclined at the angle $\bar{\theta} = \bar{\theta}_{\mathrm{n}} \approx 24.09°$ and corresponding to elastic neutrality: (a) the elastic state is unaffected by the inclusion up to just before damage initiation ($\bar{u}_y = 0.065\bar{U}$); (b) inelastic strain initiates damage concentration at the tips of the inclusion after damage initiation ($\bar{u}_y = 0.085\bar{U}$); and (c) a complex shear band pattern has emerged at the final imposed displacement $\bar{u}_y = \bar{U}$.

et al., 2008) and experimental results showing that deformation localizes along narrow regions in soft matrix materials, where nucleation occurs at the tips of hard inclusions. These experiments have been performed on Cu-W laminates (Özturk et al., 1991), PMMA (Misra and Mandal, 2007) or epoxy resin (Bigoni et al., 2008) matrices containing metal inclusions.

Shear bands formation and growth from a RLI inclined at the angle of neutrality, $\bar{\theta} = \bar{\theta}_{\mathrm{n}} \approx 24.09°$, for purely elastic behaviour and with Poisson's ratio $\nu_{\mathrm{b}} = 0.2$, is analyzed in Fig. 10, where the damage field ω is shown at three stages of imposed displacements $\bar{u}_y = \{0.065, 0.085, 1\}\bar{U}$ (increasing from left to right). As a consequence of the elastic neutrality, the inclination of the inclusion is such that stress singularities are not activated during the elastic response and therefore the solution field remains homogeneous (Fig. 10(a)) until the yield stress is simultaneously reached at every point of the domain. Remarkably, the inelastic and incrementally anisotropic response of the material induces a stress concentration at each inclusion tip (Fig. 10(b)), promoting a non-symmetric shear-band formation (Fig. 10(c)).

4.2. Two interacting RLIs

Shear bands that originate from the interaction of two RLIs of equal half-length $a = L/13$ and inclined at different reciprocal angles are analyzed. Boundary conditions and material parameters are the same as those specified in Section 4.1. Results in terms of maps of the damage parameter ω are reported in Fig. 11. Two cases with only one RLI are included in this figure (panels (d) and (f)) as a reference to facilitate the discussion on the influence of a second RLI.

As shown in Fig. 11, each inclusion is centered in the corresponding vertical half of the square domain, therefore the distance between their midpoints is equal to $L/2$. The RLIs' inclination is selected from a set of various angles: $\bar{\theta} = 90°$ (i.e. parallel to the y-axis), $\bar{\theta} = 0°$ (i.e. parallel to the x-axis), $\bar{\theta} = \bar{\theta}_{\mathrm{n}} \approx 24.09°$ (corresponding to the angle of elastic neutrality), and $\bar{\theta} = 50°$. At variance with the rest of the analyses presented in this section, $\bar{\sigma}_0/E_{\mathrm{b}} = 3 \times 10^{-4}$ has been assumed.

The following conclusions can be drawn from an analysis of Fig. 11.

- All panels show localization of damage arranged into narrow zones with dominant inclinations $\theta_{\mathrm{sb}}^{(\pm)} \approx \pm 37°$ (these are also the inclinations of the shear bands emanating from an imperfection as shown in Fig. 12).

Published in *International Journal of Solids and Structures* (2021) **210–211**, 255-272
doi: https://doi.org/10.1016/j.ijsolstr.2020.11.006

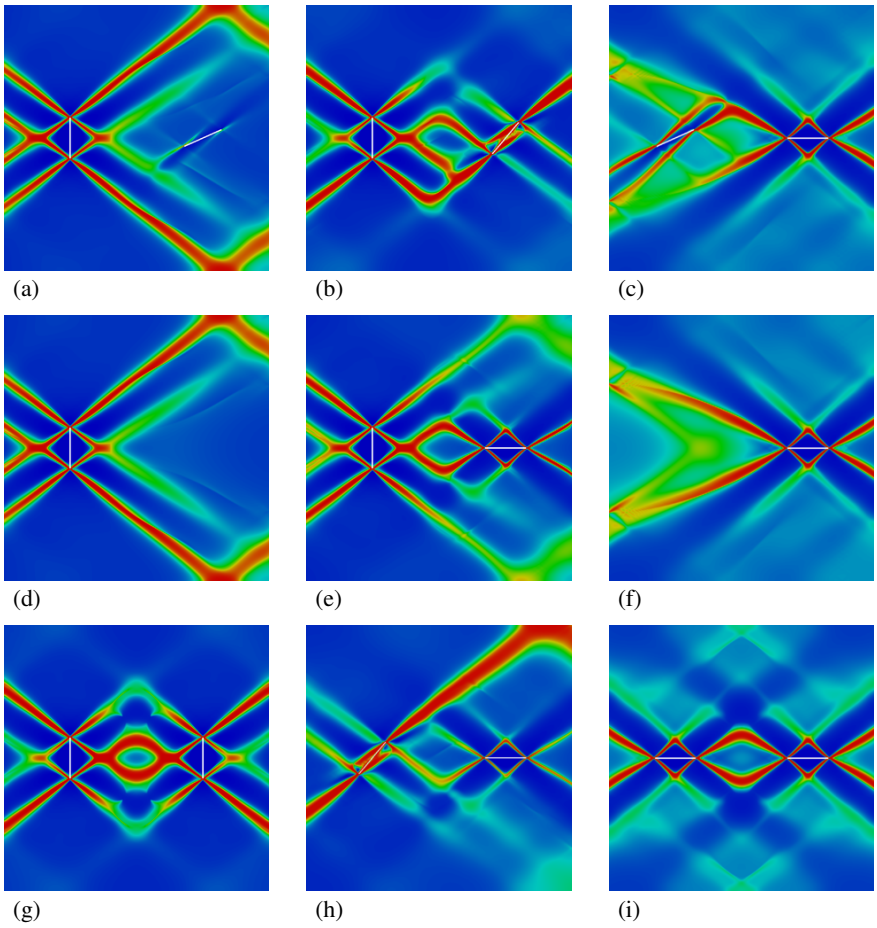

Figure 11: Localization of damage ω showing shear bands originating from the interaction of two RLIs at various inclinations: (a) vertical ($\bar{\theta} = 90°$) and at neutral inclination ($\bar{\theta} = \bar{\theta}_{\mathrm{n}} \approx 24.09°$), (b) vertical ($\bar{\theta} = 90°$) and inclined at $\bar{\theta} = 50°$, (c) neutral ($\bar{\theta} = \bar{\theta}_{\mathrm{n}} \approx 24.09°$) and horizontal ($\bar{\theta} = 0°$), (d) only one vertical inclusion is considered, (e) vertical and horizontal, (f) only one horizontal inclusion is considered, (g) both vertical, (h) inclined at $\bar{\theta} = 50°$ and horizontal, (i) both horizontal. The two cases in panels (d) and (f) with only one inclusion have been included for comparison purposes. The color scale is the same as in Fig. 9.

Published in *International Journal of Solids and Structures* (2021) **210–211**, 255-272
doi: https://doi.org/10.1016/j.ijsolstr.2020.11.006

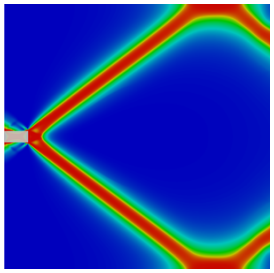

Figure 12: Map of damage field ω revealing shear bands as nucleated from an imperfection symmetrically placed along the left-hand boundary of the specimen (where RLIs are not present). The shear bands are inclined at the conjugate angles of $\theta_{\rm sb}^{(\pm)} \approx \pm 37°$ with respect to the x-axis. The color scale is the same as in Fig. 9.

- Panels (g) and (i) show the shear band patterns for the symmetric cases of two inclusions either vertical or horizontal. In both cases the shear bands geometries in each vertical half domain closely resemble those in the corresponding half domain of the reference panels (d) and (f).

- Panels (b) and (h) display an inclusion inclined at $\bar{\theta} = 50°$ interacting, respectively, with another vertical or horizontal inclusion. In both cases, a strong damage localization arises at the tips of the inclined inclusion. The widths of the bands is comparable to that of the bands arising from the vertical inclusion in panel (b), but considerably wider than that of the horizontal inclusion in panel (h).

- Panels (a) and (c) show the effect of an inclusion placed at the elastic neutrality angle, $\bar{\theta} = \bar{\theta}_{\rm n} \approx 24.09°$, interacting, respectively, with another vertical or a horizontal inclusion. In panel (a) the inclined inclusion is 'shielded' by two strong shear bands emanating from the vertical inclusion so that the inclined inclusion leaves the pattern generated by the other inclusion almost unperturbed (compare with panel (d)). The situation is different for panel (c), where the inclined inclusion 'attracts' one of the shear bands originating from the horizontal inclusion so that the global pattern results modified with respect to that related to panel (f).

- Consider the two cases with a single RLI in panels (d) and (f) and the corresponding vertical halves of the square domain containing the RLI. The shear bands emanating from the RLI in these halves are approximately comparable to the shear bands emanating from similarly-oriented RLIs in their corresponding halves in all other panels. This indicates that, for the considered RLIs dimension and distance, the shear band pattern of each RLI is locally preserved. For example, panel (e) shows a shear band pattern that can be closely approximated by superimposing results taken from the halves containing the RLI in reference panels (d) and (f).

  This observation is strictly related to the presence of RLIs with comparable length. Indeed, as shown later in Section 4.4, when RLIs with different lengths are present, shear bands emerging from longer RLIs prevail over those related to shorter ones.

4.3. Shear bands nucleated from an imperfection and their interaction with RLIs

This section is dedicated to the study of the interaction of the shear bands nucleated from an imperfection with the surrounding RLIs, where the imperfection can be interpreted as an agent disturbing an otherwise uniform specimen. We consider the cases of one, two, and 1500 RLIs. The imperfection is introduced as

Published in *International Journal of Solids and Structures* (2021) **210–211**, 255-272
doi: https://doi.org/10.1016/j.ijsolstr.2020.11.006

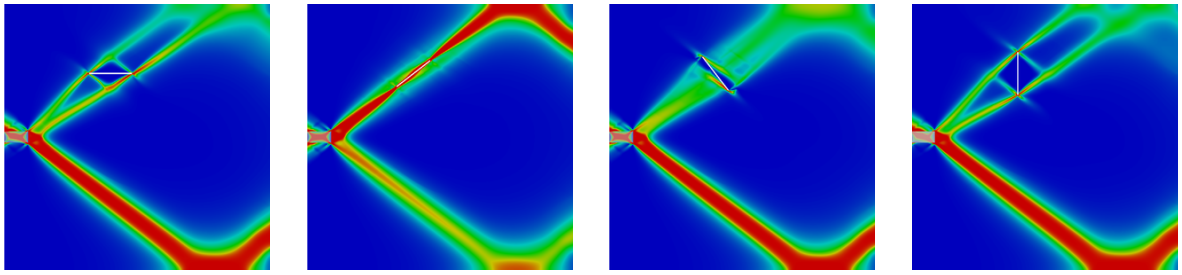

Figure 13: Maps of damage field ω revealing interaction of the shear bands nucleated from an imperfection (located at the middle of the left edge of the boundary) with a RLI placed at varying inclinations. The color scale is the same as in Fig. 9.

a rectangular region ($0.0425L \times 0.09L$) whose material is characterized by reduced values of yield stress σ_0 and Young's modulus E_b^{2D} with respect to bulk material values, and is symmetrically placed along the left-hand boundary of a square domain of size L. The bulk material properties are defined at the beginning of Section 4, and the square domain is subject to the boundary conditions specified in Section 4.1. The imperfection generates a symmetric damage field that defines a set of reference shear bands inclined at the conjugate angles of $\theta_{sb}^{(\pm)} \approx \pm 37°$ with respect to the x-axis (Fig. 12).

4.3.1. Interaction with one or two RLIs

Changes in the damage fields are investigated when one or two RLIs, with varying inclination and length, are placed approximately at the middle of one of the reference shear bands.

Figure 13 shows the effect of a single inclusion of half-length $a = 0.08L$ at different inclinations ($\bar{\theta}^{[1]} = \{0, 37, -53, 90\}°$ from panel (a) to (d)). The shear band fields in panels (a), (c), and (d) show that damage weakens along the localization line which intersects the inclusion, while it strengthens along the other shear band direction. Conversely, when the RLI is aligned with the localization line (panel (b)) the corresponding damage region remains almost unaltered, while the damage field in the other direction is almost completely deactivated.

The effect of two symmetric inclusions is shown in Fig. 14, where symmetry allows to report only the upper half of the specimen. The two inclusions are inclined at $\bar{\theta}^{[1]} = -\bar{\theta}^{[2]} = 37°$ (panels (a) to (d)) and $\bar{\theta}^{[1]} = -\bar{\theta}^{[2]} = -53°$ (panels (e) to (h)), and have different half-lengths $a = \{0.02, 0.04, 0.08, 0.16\}L$ in panels (a) and (e), (b) and (f), (c) and (g), (d) and (h), respectively. As shown in the upper row of Fig. 14, an inclusion aligned with and located on a shear band causes only a modest reduction of the shear band thickness. Differently, RLIs that orthogonally cross an unperturbed shear band direction (Fig. 12) give rise to a splitting of the shear band in two smaller shear bands nucleating from the inclusion tips (panels (e) and (f)).

Non-symmetric cases for the imperfection interacting with a pair of RLIs with varying lengths and inclinations are presented in Fig. 15. Two RLIs with the same half-length, $a = \{0.02, 0.04, 0.08, 0.16\}L$, and inclination, $\bar{\theta}^{[1]} = 37°$ and $\bar{\theta}^{[2]} = -53°$, are shown in panels (a) to (d). The inclusion aligned with the unperturbed shear band direction (in the upper half of each panel) slightly alters the damage field similarly to the corresponding symmetric case (panels (a) to (d) in Fig. 14). Conversely, the effect of the other inclusion (shown in the lower half of each panel) ranges from a split of the lower shear band into two smaller shear bands (for $a = 0.02L$, panel (a), similar to the symmetric case in Fig. 14(e)), to an annihilation of the shear band (for $a = 0.16L$, panel (d)).

Published in *International Journal of Solids and Structures* (2021) **210–211**, 255-272
doi: https://doi.org/10.1016/j.ijsolstr.2020.11.006

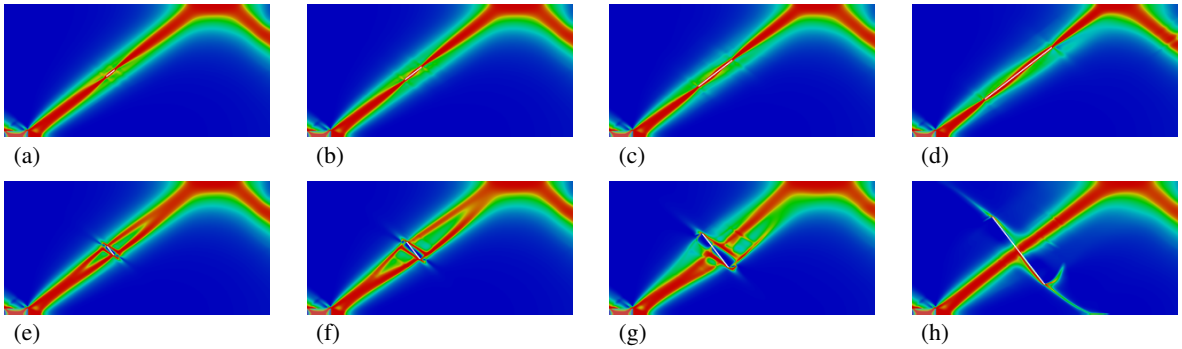

Figure 14: Maps of damage field ω revealing interaction of the shear bands nucleated from an imperfection with two symmetric RLIs of different lengths and at different inclinations. Due to symmetry, only the upper half of domain is reported. The color scale is the same as in Fig. 9.

Specimens with two RLIs of the same length but increasing from left to right are shown in the upper part of Fig. 15, where one RLI lies on the upper shear band direction and the other is orthogonal to the conjugate direction. The lower part of the figure reports the case of two RLIs of equal length ($a = 0.08L$), one lying along one shear band ($\bar{\theta}^{[1]} = 37°$) and the other crossing the other shear band at different inclinations ($\bar{\theta}^{[2]} = \{-37,\ 0,\ 37,\ 90\}°$). As in the previous case, the RLI lying on the shear band leaves the latter unperturbed (compare panels (e) to (h) in Fig. 15 with the mirror of the upper half in panel (c) of Fig. 14), while the shear band cut by the RLI is almost annihilated, except when the RLI lies on the shear band ($\bar{\theta}^{[2]} = -37°$), similar to the upper shear bands.

4.3.2. Interaction with a large number of RLIs

The failure mechanism of composites with a large number of RLIs (all with the same half-length $a = 0.02L$) is investigated by considering five of the six distributions of 1500 RLIs reported in Fig. 7 and a random distribution of 1500 RLI equally-inclined at the neutral angle. These distributions generate the shear bands patterns illustrated in Fig. 16 and are used later for comparison purposes. The strong influence of the RLIs' distribution is evident, with the generation of partially organized shear band patterns. Shear band lengths comparable to the unit cell size are observed for all but the vertical distribution (panel (c)) where these become more fragmented.

When an imperfection is also present in the specimen as in Fig. 12, the two shear bands emanating from the imperfection are 'fragmented' to varying degrees by the RLIs, as shown in Fig. 17. The fragmentation ranges from moderate (panels (a) and (b)) to severe (panels (d) and (f)), with cases of annihilation and shielding (panels (c) and (e)), leading to shear band geometries similar to the percolation patterns found for highly anisotropic solids (Bigoni and Noselli, 2010a,b; Gourgiotis and Bigoni, 2016). In all cases, the imperfection and the RLIs' distributions have a marked influence on the final shear band patterns. Even if the inclusions perturb the reference shear bands by fragmenting them, panels (a), (b), (d), and (f) show that influence regions are determined by the reference shear bands. Fragmentation of the shear bands in the remaining two cases, panels (c) and (e), is so strong that the final shear band fields result markedly different from the two macro shear bands visible in Fig. 12 and referred to a sample without RLIs. Note also that the neutral angle distribution of RLIs in panel (b) appears to be the less disruptive for the development of the macro shear bands, while the vertical distributions in panels (c) and (e) provide the maximum shielding to shear band growth.

Published in *International Journal of Solids and Structures* (2021) **210–211**, 255-272
doi: https://doi.org/10.1016/j.ijsolstr.2020.11.006

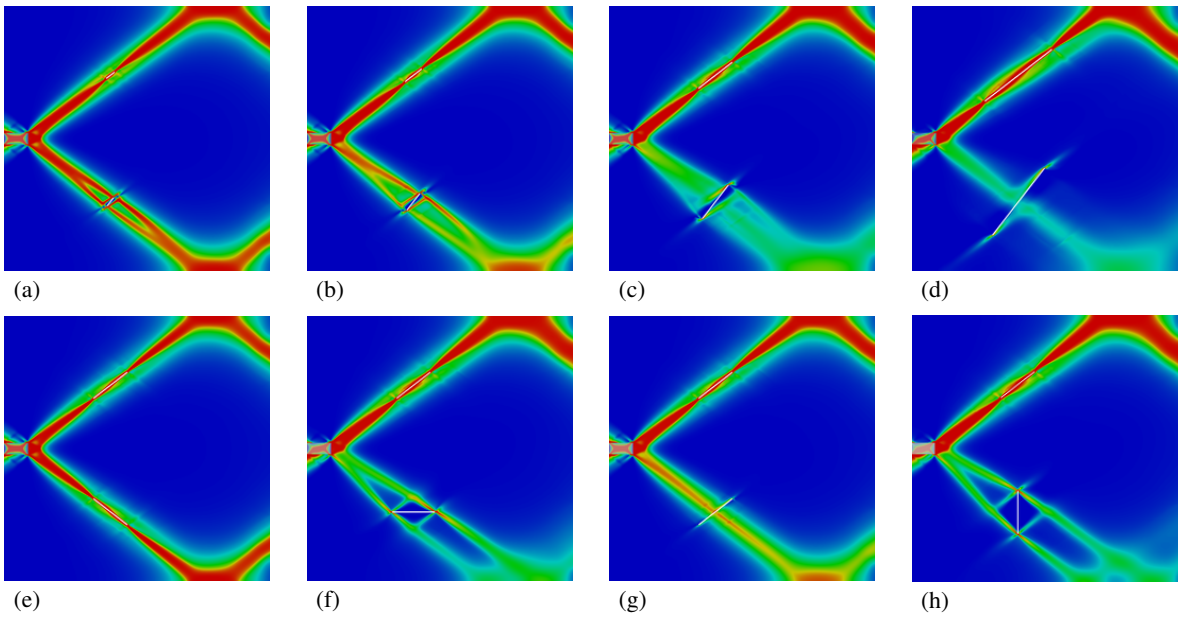

Figure 15: Maps of damage field ω revealing interaction of the shear bands nucleated from an imperfection with two RLIs with varying lengths and inclinations. The color scale is the same as in Fig. 9.

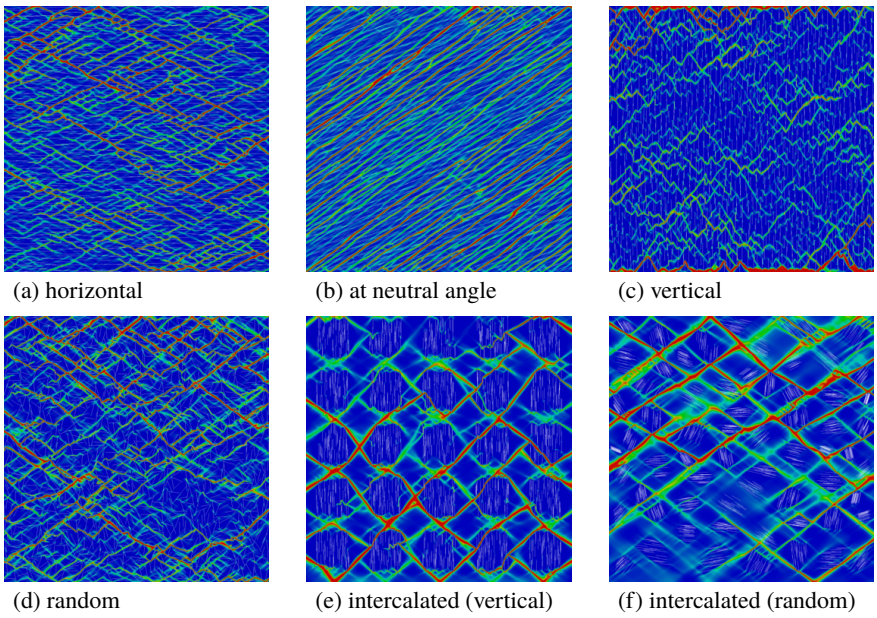

Figure 16: Maps of damage field ω revealing shear bands formation from 1500 RLIs at various distributions. RLIs are: (a) horizontal as in Fig. 7(a); (b) inclined at neutral angle $\bar{\theta} \approx 24.09°$ (in a random distribution akin to Fig. 6(a)); (c) vertical as in Fig. 7(b); and (d) randomly inclined as in Fig. 7(c); (e) intercalated vertically as in Fig. 7(d); and (f) intercalated randomly as in Fig. 7(f). The color scale is the same as in Fig. 9.

Published in *International Journal of Solids and Structures* (2021) **210–211**, 255-272
doi: https://doi.org/10.1016/j.ijsolstr.2020.11.006

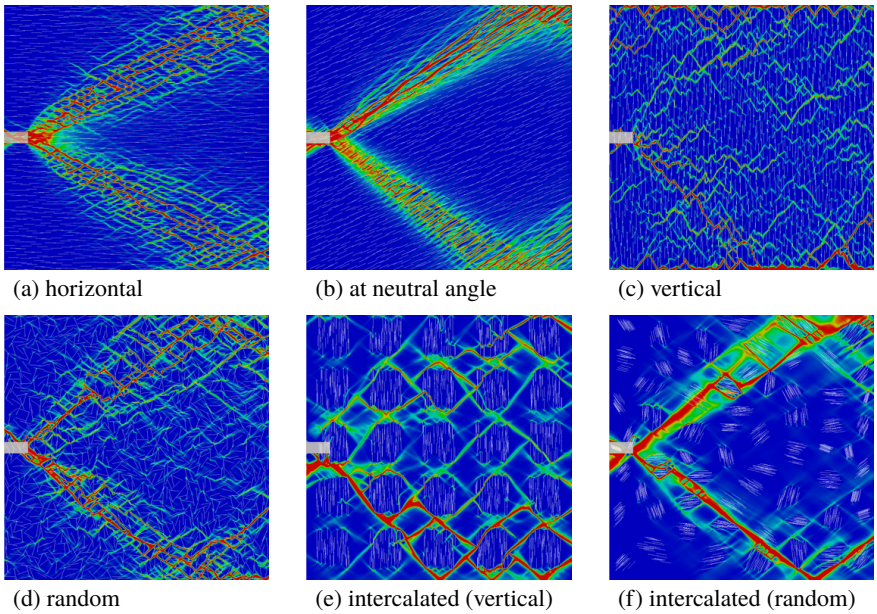

(a) horizontal (b) at neutral angle (c) vertical

(d) random (e) intercalated (vertical) (f) intercalated (random)

Figure 17: As for Fig. 16, except that now an imperfection is present on the left edge of the domain as that reported in Fig. 12, where RLIs are not present. RLIs completely change the 'double shear band geometry' visible in Fig. 12 even if the latter still defines, in panels (a) to (d), influence zones for the clusters of shear bands nucleated near the RLIs. The color scale is the same as in Fig. 9.

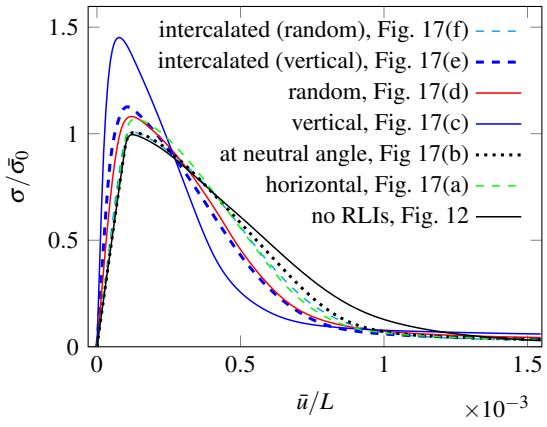

Figure 18: Influence of RLIs' distributions on the global stress/strain response for the square samples analyzed in Fig. 17. A stress normalization is introduced through division by the maximum stress $\bar{\sigma}_0$ referred to the sample without RLIs.

Published in *International Journal of Solids and Structures* (2021) **210–211**, 255-272
doi: https://doi.org/10.1016/j.ijsolstr.2020.11.006

RLI distribution	$E^{2D}_{eff,y} \Big/ E^{2D^*}_{eff,y}$	$\max(\sigma)/\max(\sigma^*)$	U_T/U_T^*
Horizontal, Fig. 17(a)	1.034	1.073	0.920
At neutral angle, Fig. 17(b)	1.005	1.010	0.929
Vertical, Fig. 17(c)	4.288	1.458	0.911
Randomly inclined, Fig. 17(d)	1.617	1.085	0.892
Intercalated (vertical), Fig. 17(e)	2.138	1.131	0.879
Intercalated (random), Fig. 17(f)	1.126	1.013	0.910

Table 1: Values of effective in-plane Young's modulus, maximum stress, and toughness obtained from the stress-strain curves in Fig. 18 normalized by the corresponding values (denoted with a star) obtained on a specimen with an imperfection but without RLIs.

To appreciate the RLIs' influence on the global response of the composite, the normalized stress-strain curves are reported in Fig. 18 for the cases just analyzed. The figure includes also the normalized stress-strain curve for a specimen with an imperfection on the left edge and without RLIs (the final damage map is reported in Fig. 12). Table 1 conveniently lists the corresponding effective in-plane Young's modulus, maximum stress, and toughness U_T. These quantities are normalized with respect to the corresponding quantities (denoted with a star) obtained from the specimen without RLIs. The toughness value U_T for a specific RLI distribution is defined as the measure of the area under the stress-strain curve from the unloaded state to $\bar{u}/L = 10^{-3}$.

RLIs' distributions affect the global response at various levels. In all examined cases, and compared to the response of the specimen without RLIs (Fig. 12), inclusions are responsible for an increase of the effective in-plane Young's modulus (in the vertical direction) and maximum stress values, together with a reduction of the toughness. The only exception is represented by the neutral distribution for which the effective in-plane Young's modulus is practically unaffected, in analogy with the observed growth of shear bands documented in Fig. 10 (the small deviation of the maximum stress from unity is due to round-off errors in the numerical evaluation). The two vertical distributions lead to highest stiffness and maximum stress values and to the lowest toughness values, although the response of the intercalated (vertical) distribution (Fig. 7(d)) is very similar to that of the other distributions.

The normalized stress-strain curves in Fig. 18 also indicate that the higher the maximum stress, the steeper the softening branch, leading to some considerations on the shear band patterns as discussed next. A visual comparison of the stress-strain curves and the corresponding shear band networks in Figs. 12 and 17 shows that the shear bands forming for RLIs aligned parallel to the neutral inclination, panel (b), are the closest to the shear bands emanating from the defect in the specimen without RLIs; the two corresponding stress-strain curves are also very close to each other. Sorting the remaining RLIs' distributions by increasing values of the maximum stress (or corresponding decreasing softening slope) yields the following list (with indication of the shear band pattern, as visible in the panels of Fig. 17): (i.) intercalated (random), panel (f); (ii.) horizontal, panel (a); (iii.) randomly inclined, panel (d); (iv.) intercalated (vertical), panel (e); (v.) vertical, panel (c). The sequence of the shear band patterns shows a clear evolution from the localized pattern in panel (b), corresponding to the neutral distribution, to the very diffuse pattern in panel (c), related to the vertical distribution.

4.4. Periodic distributions of RLIs

The analyses in Section 4.3 indicate that RLIs can be very effective in disrupting shear band patterns emanating from a large defect. In analogy with those analyses, their 'disruptive capacity' is now analyzed

Published in *International Journal of Solids and Structures* (2021) **210–211**, 255-272
doi: https://doi.org/10.1016/j.ijsolstr.2020.11.006

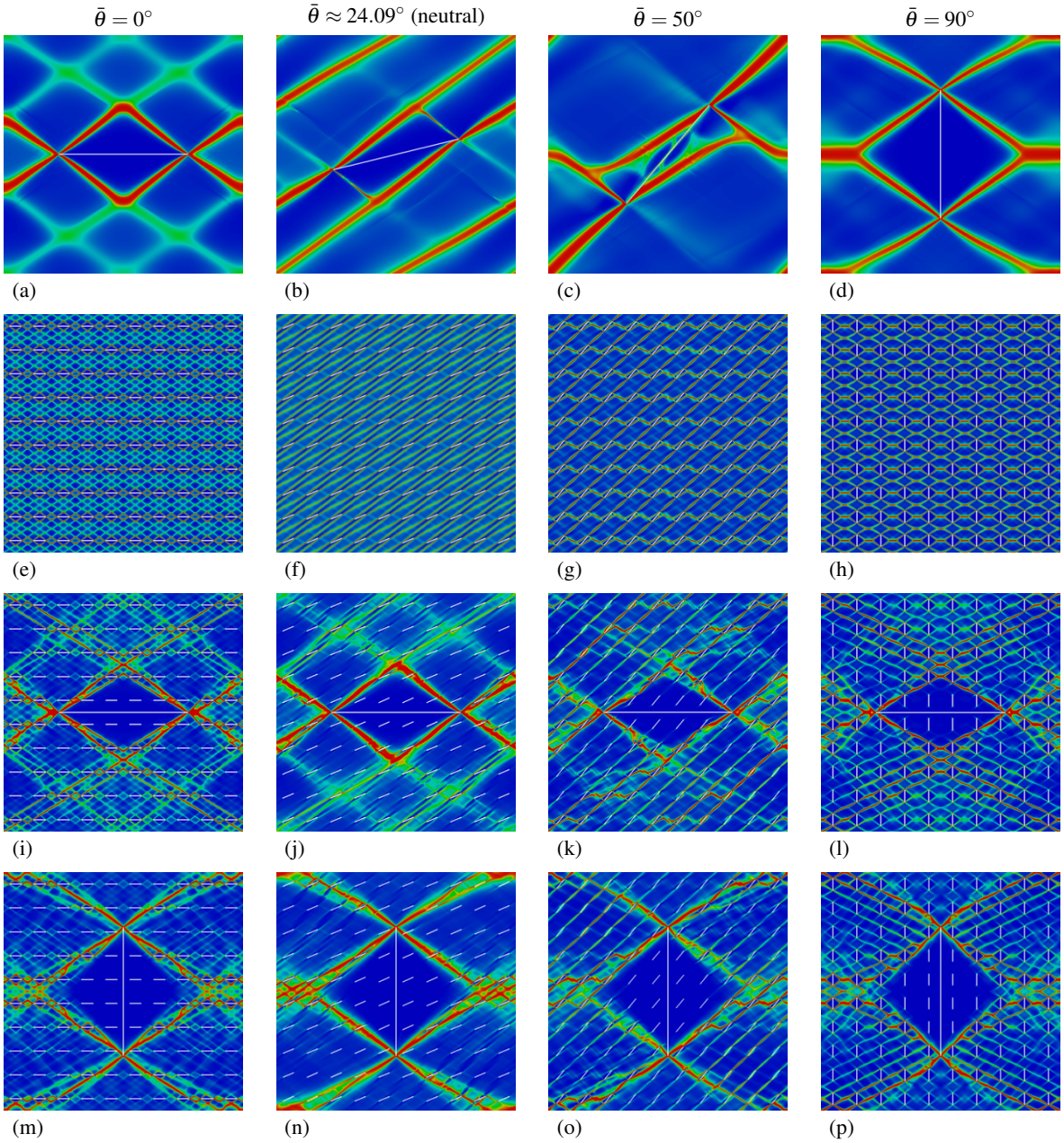

Figure 19: Maps of damage field ω revealing shear band patterns in a unit square cell (of side L) subject to macroscopic straining in the vertical direction and containing different RLIs' distributions. Upper row: one large (or 'macro') RLI ($a = L/4$); Second row: a periodic distribution of small (or 'micro') RLIs ($a = L/40$); Third row: one large horizontal RLI inside a periodic distribution of small RLIs at different inclinations ($\bar{\theta} = \{0, 24.09, 50, 90\}°$); Lower row: as in the third row, but the large RLI is vertical. The color scale is the same as in Fig. 9.

Published in *International Journal of Solids and Structures* (2021) **210–211**, 255-272
doi: https://doi.org/10.1016/j.ijsolstr.2020.11.006

for a family of small ('micro') RLIs with respect to the shear bands emanating from a large ('macro') RLI. To simulate the behaviour of an infinite domain, the RLIs are embedded in a square $L \times L$ unit cell subject to periodic boundary conditions. Small RLIs are characterized by a half-length $a_{\mathrm{m}} = L/40$ and one hundred of these is analyzed at different inclinations ($\bar{\theta}_{\mathrm{m}} = \{0, 24.09, 50, 90\}°$) while one large RLI with half-length $a_{\mathrm{M}} = L/4$ is added, in either the horizontal ($\bar{\theta}_{\mathrm{M}} = 0°$) or vertical ($\bar{\theta}_{\mathrm{M}} = 90°$) direction. The bulk material properties are defined at the beginning of Section 4.

The RLIs are embedded in a square unit cell of size L under periodic boundary conditions (Suquet, 1985). The cell is subject to macroscopic straining in the vertical direction obtained by applying a constant displacement rate using the same parameters employed in Section 4.1.

The shear bands generated by one large RLI placed at different inclinations in the center of the unit cell are visible in the upper row of Fig. 19. The second row shows the shear band patterns generated by RLIs' distributions obtained by the horizontal and vertical stacking of the corresponding distributions in the upper row (with a scale factor 0.1). Because of the periodic boundary conditions and the homothetic relation between unit cells in the upper and second rows, the shear band patters in the second row can be reconstructed from those in the upper row by means of the same procedure used to generate the RLIs' distributions.

As in the cases discussed earlier, the inclination of the RLIs dramatically influences the shear band patterns. In particular, symmetric networks involving the two conjugate shear band inclinations $\theta_{\mathrm{sb}}^{(\pm)}$ can be observed in panels (a) ($\bar{\theta} = 0°$) and (d) ($\bar{\theta} = 90°$), while the other two inclinations in panels (b) and (c) generate non-symmetric networks, with localization developing mainly at inclination $\theta_{\mathrm{sb}}^{(+)}$. A third further shear band inclination is visible in panel (c), close to that of the RLI.

The interaction between micro and macro RLIs is illustrated by considering a macro RLI placed at the center of the unit cell and inclined at $\bar{\theta}_{\mathrm{M}}$, while surrounded by arrays of micro RLIs inclined at $\bar{\theta}_{\mathrm{m}}$. Maps of damage localization are reported for eight combinations of micro and macro RLIs in the third ($\bar{\theta}_{\mathrm{M}} = 0°$) and fourth ($\bar{\theta}_{\mathrm{M}} = 90°$) row of Fig. 19. These fields clearly show the strong mutual influence between micro and macro inclusions. In particular, the array of micro RLIs generates a fragmentation of the macro-pattern shear band fields in a manner specific to each micro RLI inclination. This consideration does not hold for the micro RLIs at the neutral inclination $\bar{\theta} = 24.09°$, where the shear band fields closely resemble those related to the macro RLI (cases $\bar{\theta} = 0°$ and $90°$ in the upper row). In all the considered cases, the macro RLI shields the micro RLIs inside the rhomboidal domain defined by the intersection of the shear bands nucleated from the macro RLI tips. In this domain damage is practically zero, with very low damage levels observed around the micro RLIs close to the delimiting shear bands. Outside the shielded rhomboidal domain, the damage fields reveal micro-shear banding around the micro RLIs (except for the neutral inclination case). This observation suggests that shear bands emanating from longer RLIs prevail over those emanating from shorter RLIs, in contrast with the limit case of RLIs of equal length (Fig. 11), where the shear bands emanating from each RLI are in 'equilibrium' and none prevails over the other one.

5. Summary

Simulations performed with a two-dimensional model for the analysis of dispersions of stiff and thin platelets embedded in a ductile matrix have revealed the complex shear banding patterns leading a material to failure. The model is based on the rigid line inclusion concept, which has been applied in a visco-plastic-damaging material matrix and implemented through an embedded reinforcement approach. The embedded approach adopted in this study, based on the formulation proposed by Balakrishnan and Murray (1986),

enables an accurate and computationally affordable analysis of composites with any distribution and at any volume fraction of rigid line inclusions. Thanks to the individual representation of each inclusion by means of an appropriate kinematic description, RLIs' interaction and orientation effects are properly accounted for in the prediction of local stress fields in linear and nonlinear regimes, allowing for damage accumulation and localization at the level of each RLI.

The following results have been obtained by running analyses, with up to 1500 RLIs, for random, periodic, or clustered RLIs' distributions.

- In the elastic range, RLIs lead to a stiffening of the elastic response, with the exception occurring when the inclination of the RLIs with respect to the applied stress is sufficiently close to the 'neutrality condition' expressed by Eq. (33). The stiffening, as expected, depends on the geometry of the RLIs' distribution.

- Neutrality does not hold when the matrix material enters the inelastic regime, and therefore RLIs always have an important effect on the overall mechanical response.

- When inelastic deformation occurs and damage tends to localize into shear bands, the tips of the RLI promote, with their stress concentration, localization nucleation and growth and, at the same time, may hinder, slow down, and even stop a localization growing from a defect larger than the RLI. In the former case, shear bands form networks of more or less pronounced regularity, characterized by a fine texture modulated by the RLIs' and shear band geometries. In the latter case, the thick shear bands that would nucleate and grow from the large defect are 'fragmented' into a cascade of tiny lines of concentrated damage, often following a path coherent with the thick, undeveloped underlying shear bands.

Acknowledgments

The research leading to these results has received funding from the European Research Council under the European Union's Seventh Framework Programme (FP7/2007-2013) / ERC Grant agreement n° 617972 (MG and AS). FDC and DB gratefully acknowledge financial support from the Italian Ministry of Education, Universities and Research (MIUR) through the grant PROSCAN (MIUR-ARS01_01384).

DB and FDC acknowledge the profound and fruitful cooperation through these years with Professor Henryk Petryk. His penetrating view of mechanics has provided them many insights and inspirations. They look forward to many more years of enjoying stimulating scientific and human interactions with him.

References

G. Alzetta and L. Heltai. Multiscale modeling of fiber reinforced materials via non-matching immersed methods. *Computers & Structures*, 239:106334, 2020.

L. Argani, D. Bigoni, and G Mishuris. Dislocations and inclusions in prestressed metals. *Proceedings of the Royal Society A: Mathematical, Physical and Engineering Sciences*, 469(2154):20120752, 2013.

C. Atkinson. Some ribbon-like inclusion problems. *International Journal of Engineering Science*, 11(2): 243–266, 1973.

C. Atkinson and R. V. Craster. Theoretical aspects of fracture mechanics. *Progress in Aerospace Sciences*, 31 (1):1–83, 1995.

F. Auricchio, G. Scalet, and P. Wriggers. Fiber-reinforced materials: finite elements for the treatment of the inextensibility constraint. *Computational Mechanics*, 60(6):905–922, 2017.

S. Balakrishnan and D. W. Murray. Finite element prediction of reinforced concrete behavior. Structural Engineering Report No. 138, Department of Civil Engineering, University of Alberta, Edmonton, Alberta, Canada, 1986.

S. Baranova, S. G. Mogilevskaya, V. Mantič, and S. Jiménez-Alfaro. Analysis of the antiplane problem with an embedded zero thickness layer described by the Gurtin-Murdoch model. *Journal of Elasticity*, 140: 171–195, 2020.

E. Barbieri and N. M. Pugno. A computational model for large deformations of composites with a 2D soft matrix and 1D anticracks. *International Journal of Solids and Structures*, 77:1–14, 2015.

F. Barzegar and S. Maddipudi. Three-dimensional modeling of concrete structures. II: Reinforced concrete. *Journal of Structural Engineering*, 123(10):1347–1356, 1997.

D. Bigoni. *Nonlinear solid mechanics: Bifurcation theory and material instability*. Cambridge University Press, 2012.

D. Bigoni and G. Noselli. Localized stress percolation through dry masonry walls. Part I–Experiments. *European Journal of Mechanics-A/Solids*, 29(3):291–298, 2010a.

D. Bigoni and G. Noselli. Localized stress percolation through dry masonry walls. Part II–Modelling. *European Journal of Mechanics-A/Solids*, 29(3):299–307, 2010b.

D. Bigoni and H. Petryk. A note on divergence and flutter instabilities in elastic plastic materials. *International Journal of Solids and Structures*, 39(4):911–926, 2002.

D. Bigoni, F. Dal Corso, and M. Gei. The stress concentration near a rigid line inclusion in a prestressed, elastic material. Part II: Implications on shear band nucleation, growth and energy release rate. *Journal of the Mechanics and Physics of Solids*, 56(3):839–857, 2008.

J. E. Bolander and S. Saito. Discrete modeling of short-fiber reinforcement in cementitious composites. *Advanced Cement Based Materials*, 6(3):76–86, 1997.

J. Chatterjee, F. Ma, D. P. Henry, and P. K. Banerjee. Advanced boundary element analysis of three-dimensional elastic solids with fiber reinforcements. *Journal of Engineering Mechanics*, 134(9):739–749, 2008.

R. A. Chaudhuri. Three-dimensional singular stress/residual stress fields at crack/anticrack fronts in monoclinic plates under antiplane shear loading. *Engineering Fracture Mechanics*, 87:16–35, 2012.

R. A. Chaudhuri and S.-H. J. Chiu. Three-dimensional singular stress field near the interfacial bond line of a tapered jointed plate either free-standing (notch) or (fully/partially) attached to a super-rigid inclusion (antinotch). *Engineering Fracture Mechanics*, 91:87–102, 2012.

Y. Z. Chen. Singular behaviour at fixed rigid line tip in plane elasticity. *Engineering Fracture Mechanics*, 25 (1):11–16, 1986.

Y. Z. Chen. Investigation of stress singularity coefficient for a finite plate containing rigid line. *Engineering Fracture Mechanics*, 40(1):17–24, 1991.

G. P. Cherepanov. The propagation of cracks in a continuous medium. *Journal of Applied Mathematics and Mechanics*, 31(3):503–512, 1967.

T. W. Clyne and D. Hull. *An Introduction to Composite Materials*. Cambridge University Press, 2019.

T. W. Clyne and P. J. Withers. *An Introduction to Metal Matrix Composites*. Cambridge University Press, 1995.

V. M. C. F. Cunha, J. A. O. Barros, and J. M. Sena-Cruz. A finite element model with discrete embedded elements for fibre reinforced composites. *Computers & Structures*, 94–95:22–33, 2012.

G. Cusatis, D. Pelessone, and A. Mencarelli. Lattice Discrete Particle Model (LDPM) for failure behavior of concrete. I: Theory. *Cement and Concrete Composites*, 33(9):881–890, 2011.

F. Dal Corso and D. Bigoni. The interactions between shear bands and rigid lamellar inclusions in a ductile metal matrix. *Proceedings of the Royal Society A: Mathematical, Physical and Engineering Sciences*, 465 (2101):143–163, 2009.

F. Dal Corso, D. Bigoni, and M. Gei. The stress concentration near a rigid line inclusion in a prestressed, elastic material. Part I: Full-field solution and asymptotics. *Journal of the Mechanics and Physics of Solids*, 56(3):815–838, 2008.

F. Dal Corso, S. Shahzad, and D. Bigoni. Isotoxal star-shaped polygonal voids and rigid inclusions in nonuniform antiplane shear fields. Part I: Formulation and full-field solution. *International Journal of Solids and Structures*, 85:67–75, 2016a.

F. Dal Corso, S. Shahzad, and D. Bigoni. Isotoxal star-shaped polygonal voids and rigid inclusions in nonuniform antiplane shear fields. Part II: Singularities, annihilation and invisibility. *International Journal of Solids and Structures*, 85:76–88, 2016b.

C. Y. Dong and K. Y. Lee. Numerical analysis of doubly periodic array of cracks/rigid-line inclusions in an infinite isotropic medium using the boundary integral equation method. *International Journal of Fracture*, 133(4):389–405, 2005.

A. E. Elwi and T. M. Hrudey. Finite element model for curved embedded reinforcement. *Journal of Engineering Mechanics*, 115(4):740–754, 1989.

M. Goudarzi and A. Simone. Discrete inclusion models for reinforced composites: Comparative performance analysis and modeling challenges. *Computer Methods in Applied Mechanics and Engineering*, 355:535–557, 2019.

P. A. Gourgiotis and D. Bigoni. Stress channelling in extreme couple-stress materials Part II: Localized folding vs faulting of a continuum in single and cross geometries. *Journal of the Mechanics and Physics of Solids*, 88:169–185, 2016.

L. J. Hall, V. R. Coluci, D. S. Galvão, M. E. Kozlov, M. Zhang, S. O. Dantas, and R. H. Baughman. Sign change of Poisson's ratio for carbon nanotube sheets. *Science*, 320(5875):504–507, 2008.

J. C. Halpin. Effects of environmental factors on composite materials. Technical report, US Air Force Material Laboratory, AFML-TR-67-423, 1969.

H. Hartl. *Development of a continuum-mechanics-based tool for 3D finite element analysis of reinforced concrete structures and application to problems of soil-structure interaction*. PhD thesis, Graz University of Technology, 2002.

K. Hu, D. D. Kulkarni, I. Choi, and V. V. Tsukruk. Graphene-polymer nanocomposites for structural and functional applications. *Progress in Polymer Science*, 39(11):1934–1972, 2014.

J. W. Ju. On energy-based coupled elastoplastic damage theories: Constitutive modeling and computational aspects. *International Journal of Solids and Structures*, 25(7):803–833, 1989.

Y. Kojima, A. Usuki, M. Kawasumi, A. Okada, Y. Fukushima, T. Kurauchi, and O. Kamigaito. Mechanical properties of nylon 6-clay hybrid. *Journal of Materials Research*, 8(5):1185–1189, 1993.

J. Kozicki and J. Tejchman. Effect of steel fibres on concrete behavior in 2D and 3D simulations using lattice model. *Archives of Mechanics*, 62:1–28, 2010.

W. J. Landis. The strength of a calcified tissue depends in part on the molecular structure and organization of its constituent mineral crystals in their organic matrix. *Bone*, 16(5):533–544, 1995.

B. Liu, L. Zhang, and H. Gao. Poisson ratio can play a crucial role in mechanical properties of biocomposites. *Mechanics of Materials*, 38(12):1128–1142, 2006a.

J. Liu, W-J Boo, A. Clearfield, and H-J Sue. Intercalation and exfoliation: A review on morphology of polymer nanocomposites reinforced by inorganic layer structures. *Materials and Manufacturing Processes*, 21(2):143–151, 2006b.

H. R. Lusti and A. A. Gusev. Finite element predictions for the thermoelastic properties of nanotube reinforced polymers. *Modelling and Simulation in Materials Science and Engineering*, 12(3):S107, 2004.

S. Misra and N. Mandal. Localization of plastic zones in rocks around rigid inclusions: Insights from experimental and theoretical models. *Journal of Geophysical Research: Solid Earth*, 112(B9), 2007.

D. Misseroni, F. Dal Corso, S. Shahzad, and D. Bigoni. Stress concentration near stiff inclusions: Validation of rigid inclusion model and boundary layers by means of photoelasticity. *Engineering Fracture Mechanics*, 121:87–97, 2014.

T. Mori and K. Tanaka. Average stress in matrix and average elastic energy of materials with misfitting inclusions. *Acta Metallurgica*, 21(5):571–574, 1973.

L. Ni and S. Nemat-Nasser. A general duality principle in elasticity. *Mechanics of Materials*, 24(2):87–123, 1996.

N. Nishimura and Y. J. Liu. Thermal analysis of carbon-nanotube composites using a rigid-line inclusion model by the boundary integral equation method. *Computational Mechanics*, 35(1):1–10, 2004.

G. Noselli, F. Dal Corso, and D. Bigoni. The stress intensity near a stiffener disclosed by photoelasticity. *International Journal of Fracture*, 166(1):91–103, 2010.

T. Özturk, W. J. Poole, and J. D. Embury. The deformation of Cu-W laminates. *Materials Science and Engineering: A*, 148(2):175–178, 1991.

H. Petryk. On constitutive inequalities and bifurcation in elastic-plastic solids with a yield-surface vertex. *Journal of the Mechanics and Physics of Solids*, 37:265–299, 1989.

H. Petryk. The energy criteria of instability in time-independent inelastic solids. *Archives of Mechanics*, 43: 519–545, 1991.

H. Petryk. Material instability and strain-rate discontinuities in incrementally nonlinear continua. *Journal of the Mechanics and Physics of Solids*, 40:1227–1250, 1992.

H. Petryk. Plastic instability: Criteria and computational approaches. *Archives of Computational Method in Engineering*, 4:111–151, 1997.

H. Petryk. General conditions for uniqueness in materials with multiple mechanisms of inelastic deformation. *Journal of the Mechanics and Physics of Solids*, 48:367–396, 2000.

H. Petryk. A quasi-extremal energy principle for non-potential problems in rate-independent plasticity. *Journal of the Mechanics and Physics of Solids*, 136:103691–1–22, 2020.

H. Petryk and S. Stupkiewicz. Instability of equilibrium of evolving laminates in pseudo-elastic solids. *International Journal of Nonlinear Mechanics*, 47:317–330, 2012.

O. Pierard, C. Friebel, and I. Doghri. Mean-field homogenization of multi-phase thermo-elastic composites: A general framework and its validation. *Composites Science and Technology*, 64(10-11):1587–1603, 2004.

M. G. Pike and C. Oskay. XFEM modeling of short microfiber reinforced composites with cohesive interfaces. *Finite Elements in Analysis and Design*, 106:16–31, 2015.

M. G. Pike, M. A. Hickman, and C. Oskay. Interactions between multiple enrichments in extended finite element analysis of short fiber reinforced composites. *International Journal for Multiscale Computational Engineering*, 13(6), 2015.

P. Pingle, J. Sherwood, and L. Gorbatikh. Properties of rigid-line inclusions as building blocks of naturally occurring composites. *Composites Science and Technology*, 68(10):2267–2272, 2008.

P. S. Pingle, L. Gorbatikh, and J. A. Sherwood. Analysis of multiple rigid-line inclusions for application to bio-materials. In *Proceedings of IMECE2007, ASME International Mechanical Engineering Congress and Exposition, Seattle, Washington, USA*, pages 801–807, 2007.

F. K. F. Radtke, A. Simone, and L. J. Sluys. A partition of unity finite element method for obtaining elastic properties of continua with embedded thin fibres. *International Journal for Numerical Methods in Engineering*, 84(6):708–732, 2010.

J. R. Rice. A path independent integral and the approximate analysis of strain concentration by notches and cracks. *Journal of Applied Mechanics*, 35(2):379–386, 1968.

S. E Sanborn and J. H. Prévost. Discrete modeling of crack bridging by a discontinuous platelet with a controlled interface. *International Journal of Solids and Structures*, 45(18–19):5059–5073, 2008.

N. Sheng, M. C. Boyce, D. M. Parks, G. C. Rutledge, J. I. Abes, and R. E. Cohen. Multiscale micromechanical modeling of polymer/clay nanocomposites and the effective clay particle. *Polymer*, 45(2):487–506, 2004.

A. Simone and L. J. Sluys. The use of displacement discontinuities in a rate-dependent medium. *Computer Methods in Applied Mechanics and Engineering*, 193(27):3015–3033, 2004.

S. Stankovich, D. A. Dikin, G. H. B. Dommett, K. M. Kohlhaas, E. J. Zimney, E. A. Stach, R. D. Piner, SB. T. Nguyen, and R. S. Ruoff. Graphene-based composite materials. *Nature*, 442(7100):282–286, 2006.

P. M. Suquet. Elements of homogenization for inelastic solid mechanics. In E. Sanchez-Palencia and A. Zaoui, editors, *Homogenization Techniques for Composite Media*, volume 272, pages 193–278. Springer-Verlag, 1985.

X. Wang and P. Schiavone. Asymptotic elastic fields near an interface anticrack tip. *Acta Mechanica*, 230 (12):4385–4389, 2019.

Z. Y. Wang, H. T. Zhang, and Y. T. Chou. Characteristics of the elastic field of a rigid line inhomogeneity. *Journal of Applied Mechanics*, 52(4):818–822, 1985.

A. Yaghoobi and M. G. Chorzepa. Meshless modeling framework for fiber reinforced concrete structures. *Computers & Structures*, 161:43–54, 2015.

J. Zhang, J. Eisenträger, S. Duczek, and C. Song. Discrete modeling of fiber reinforced composites using the scaled boundary finite element method. *Composite Structures*, 235:111744, 2020.

O. C. Zienkiewicz and R. L. Taylor. *The Finite Element Method*. McGraw-Hill Book Company, Berkshire, fourth edition, 1989.

O. C. Zienkiewicz, D. R. J. Owen, D. V. Phillips, and G. C. Nayak. Finite element methods in the analysis of reactor vessels. *Nuclear Engineering and Design*, 20(2):507–541, 1972.